Construction of a Time-Averaged Crossed Optical Dipole Trap for Ultracold ^{6}Li Atoms

Yudong Sun

MAX PLANCK INSTITUTE
OF QUANTUM OPTICS

FermiQP

München 2022

Aufbau einer gekreuzten optischen Dipolfalle für ultrakalte ^{6}Li Atome mit zeitlicher Mittelung

Yudong Sun

Bachelorarbeit
an der Fakultät für Physik
der Ludwig–Maximilians–Universität
München

vorgelegt von
Yudong Sun

München, den 31. August 2022

Betreut von
Prof. Dr. Immanuel Bloch, Dr. Philipp Preiß und Dr. Timon Hilker
am Max-Planck-Institut für Quantenoptik

Construction of a Time-Averaged Crossed Optical Dipole Trap for Ultracold ^{6}Li Atoms

Yudong Sun

Bachelor Thesis
Faculty of Physics
Ludwig–Maximilians–University of Munich

submitted by
Yudong Sun

Munich, 31st August 2022

Supervised by
Prof. Dr. Immanuel Bloch, Dr. Philipp Preiß, and Dr. Timon Hilker
at the Max Planck Institute of Quantum Optics

Abstract

The use of ultracold neutral atoms for quantum computing and quantum simulation offers many advantages in terms of scalability. The Fermion Quantum Processor (FermiQP) experiment aims to use ultracold fermionic ^{6}Li atoms to construct a novel combined digital- and analogue quantum processor. In this thesis, a crossed-beam optical dipole trap (ODT), implemented using a 200 W, red detuned (1070 nm) laser, is proposed for use in the experiment. Trap geometries larger than the size of the focused beam are to be achieved through spatial modulation in the MHz regime using an acousto-optic modulator (AOM). The feasibility of the proposal was tested with a proof-of-concept setup built with a lower-power 1064 nm laser. A time-averaged potential with a vertical cross-sectional area approximately three times that of the static beam was attained by modulating the beam position at 3.4 MHz. By dynamically changing the shape of the time-averaged potential, the proposed ODT promises more efficient loading and faster evaporative cooling that would reduce the cycle time of the experiment as compared to a static crossed ODT.

Zusammenfassung

Ultrakalte neutrale Atome als Plattform für Quantum Computing und Quantensimulationen stechen aufgrund ihrer Skalierbarkeit hervor. Das Fermion-Quantenprozessor-Experiment (FermiQP) hat sich zum Ziel gesetzt, einen auf ultrakalten neutralen ^{6}Li-Atomen basierenden experimentellen Aufbau zu realisieren, der die Funktionen eines digitalen und eines analogen Quantencomputers vereinigt. In dieser Arbeit wird eine optische Dipolfalle, die mittels eines rot-verstimmten 200 W-Lasers (1070 nm) implementiert werden soll, vorgestellt. Fallengeometrien größer als der Strahldurchmesser im Fokus sollen durch räumliche Modulation im MHz-Regime mittels eines akusto-optischen Modulators ermöglicht werden. Die Durchführbarkeit des Vorhabens wurde mit einem Aufbau, der mit einem 1064 nm-Laser mit niedrigerer Leistung betrieben wurde, getestet. Mittels Modulation der Strahlposition mit 3,4 MHz wurde ein zeitlich gemitteltes Potential mit einer vertikalen Querschnittsfläche erreicht, die ungefähr drei mal so groß wie die ohne Modulation erreichbare Querschnittsfläche ist. Durch dynamische Variation der Form des zeitlich gemittelten Potentials werden ein effizienteres Beladen und ein schnelleres Verdampfungskühlen als mit einer statischen Dipolfalle möglich, wodurch die Zeit eines Experimentdurchlaufs reduziert werden kann.

Contents

List of Figures

Chapter 1

Introduction

"Nature isn't classical, dammit, and if you want to make a simulation of nature, you'd better make it quantum mechanical" - Feynman, 1982 [1]

1.1 Quantum Simulation and Quantum Computing

Quantum simulators aim to study complex quantum systems through the simulation of similar, but more controlled, ones. However, despite the possibility of using existing classical computers for this purpose, the time and memory required for the simulation of arbitrary quantum systems on classical ones is exponential in the size of the simulated quantum system, thereby remaining a challenge even for today's supercomputers [2]. Hence, the potential of large-scale quantum simulations built on quantum systems far exceeds the computing capabilities of classical systems.

First proposed in 1980 by Manin [3] and subsequently in 1982 by Feynman [1], these quantum simulators are often called an analogue device, since the Hamiltonian of the system to be studied is directly simulated in a quantum system.

A quantum computer, on the other hand, is a controlled, programmable quantum system used to solve a wide range of computational problems that need not be formulated as a Hamiltonian. Depending on its implementation, a quantum computer can be analogue (e.g. quantum annealing [4, 5]) or digital (e.g. gate-based quantum computing [6]).

In both cases, these devices have the potential to solve ever more difficult problems previously intractable by classical computers, such as in the areas of cryptography, quantum chemistry, and computer science. As this field of research matures and attracts increasing attention, more and more technologies are being explored to realise these machines, including, but not limited to, the use of superconducting circuits [7], ultracold atoms [8], and trapped ions [9].

1.2 FermiQP

The idea of using cold neutral atoms in an optical lattice for quantum simulation [10] and quantum computing [11, 12, 13] dates back to the turn of the 21st century. Ever since then, the technologies required for the successful implementation of such a system have become much more established. One of the projects working to implement such a cold atom-based quantum computer is the Fermion Quantum Processor (FermiQP) experiment.

The FermiQP experiment aims to develop a novel quantum processor based on ultracold fermionic ^{6}Li atoms. Since cold atoms in optical lattices are suitable for both analogue quantum simulations and digital quantum computation, this experiment aims to build a machine that combines both of the aforementioned modes of operation.

One of the major advantages of using cold atoms as qubits remains the scalability of the system. While other technologies are still only able to realise quantum computers using tens of qubits [2], the use of ultracold atoms in optical lattices easily scales up to the hundreds or thousands of qubits. In fact, just in the first stage of the experiment, the use of around 200 qubits and more than 1000 fermions is targeted for gate-based digital quantum computing ("digital mode") and analogue quantum simulation ("analogue mode") respectively.

While the experiment is still in its infancy, the preparation procedure of the cold ^{6}Li atoms for each experimental cycle has already been planned. In order to trap ^{6}Li atoms in an optical lattice, ^{6}Li atoms will first be evaporated from an oven into a 2D magneto-optical trap (MOT). Thereafter, the atoms will be cooled in successive cooling stages starting with a 3D MOT operating on the 671 nm transition of ^{6}Li. After the 3D MOT, an average ^{6}Li atom cloud temperature of a few hundred μK is expected [14]. Subsequently, gray molasses, a method of sub-Doppler laser cooling, will be employed [15], before the atoms are loaded into the optical dipole trap (ODT). Using the ODT, evaporative cooling will be performed until quantum degeneracy is reached. This degenerate Fermi gas of ^{6}Li atoms will then be loaded into a 2D optical lattice.

Once the ^{6}Li atoms are trapped in the optical lattice, it will then be possible to use the atoms either as digital qubits ("digital mode") or as fermions for analogue quantum simulations ("analogue mode").

In this thesis, a time-averaged crossed-beam red-detuned ODT with high frequency spatial modulation in the MHz-regime, implemented using a 200 W, 1070 nm infrared laser, is proposed for the loading of atoms from the 3D MOT into the optical lattice.

With a small static beam waist, a large sweeping range may be used initially to load a large number of atoms from the 3D MOT. During the evaporative cooling process, the trap size may then be reduced dynamically to increase the density of the atoms and provide a tight confinement at the very end.

The proposed ODT thus promises more efficient loading and faster evaporative cooling of ^{6}Li atoms to create the degenerate quantum gas required for the experiment.

In chapter 2, the theoretical background behind the ODT and some of its components will be explored. In chapter 3, the various design and planning considerations that went into the ODT are detailed. Finally, in chapter 4, the experimental realisation of the ODT in the form of a proof-of-concept (PoC) setup, built using a 1064 nm diode-pumped solid-state (DPSS) laser, is presented, along with relevant results.

Chapter 2

Theoretical Background

2.1 The Optical Dipole Trap

The use of light, or electromagnetic radiation in the infrared to visible regime to attract and repel atoms and plasma was first suggested by Askar'yan in 1962 [16]. In 1970, Ashkin became the first to demonstrate optical confinement by trapping micron-sized dielectric particles in a focused laser beam at Bell Laboratories [17]. This established the foundation for what is now commonly known as the "optical tweezers". Building upon this, he then proposed the use of similar forces to build a three-dimensional trap for neutral atoms [18].

In that same year, also at Bell Laboratories, Bjorkholm et al. became the first to demonstrate that neutral atoms experienced the dipole force using near-resonant laser light [19]. Subsequently in 1986, Chu et al. finally successfully demonstrated the three-dimensional optical trap proposed by Ashkin back in 1978 [20], paving the way for rapid progress in the field of laser cooling and trapping.

In this chapter, the theory of the interaction of neutral atoms with far red-detuned laser light will be explored. This serves as the foundations for the optical dipole trap (ODT) developed in this thesis.

2.1.1 Dipole Interactions

The working principle behind the ODT is the electric dipole interactions between a neutral atom and an oscillating electric field $\mathbf{E}(t)$, which in this case is the oscillating electromagnetic field of a laser beam.

Consider the atom in a semi-classical picture, where it acts as a harmonic oscillator. An atom is made up of a positively charged nucleus and a negatively charged electron cloud around it. In an external electric field $\mathbf{E}$, these two oppositely charged components experience forces in opposing directions: the positively charged nucleus in the direction of the field, and the negatively charged electron cloud in the opposite direction of the field. This pulls these two components away from each other.

Being oppositely charged, the nucleus and the electron cloud also experience an attractive coulomb force towards each other despite being pulled away from each other, keeping the atom together.

If the external electric field $\mathbf{E}$ is not too strong, the electric forces pulling the electron cloud and the nucleus apart from each other does not overcome the coulomb force and these two opposing forces reach a stable equilibrium. This leaves the neutral atom polarised, resulting in an induced dipole moment $\mathbf{p}$, which is approximately given by [21]:

$$\mathbf{p} = \alpha \mathbf{E} \tag{2.1}$$

where α is the atomic polarisability.

For a spatially uniform electric field $\mathrm{d}\mathbf{E}$, the potential energy of the system may be described with [22]:

$$\mathrm{d}U = -\mathbf{p} \cdot \mathrm{d}\mathbf{E} = -\alpha \mathbf{E}\, \mathrm{d}\mathbf{E} \tag{2.2}$$

In an oscillating field $\mathbf{E}(t)$, it is useful to use the complex notation:

$$\tilde{\mathbf{E}}(\mathbf{r}, t) = \tilde{E_0}(\mathbf{r}) e^{i\omega t} \cdot \hat{\mathbf{e}} \tag{2.3}$$

with the complex dipole moment $\tilde{\mathbf{p}}$ and the complex polarisability $\tilde{\alpha}(\omega)$, which is a function of the driving frequency ω.

The potential that the atom experiences as a result of the aforementioned induced dipole interaction may therefore be obtained via integration of (2.2) $\int_{U(\mathcal{E}=0)}^{U(\mathcal{E}=E)} \mathrm{d}U = \int_0^E -\tilde{\alpha}\mathcal{E}\, \mathrm{d}\mathcal{E}$ [23] to obtain:

$$U_{\text{dip}} = -\frac{1}{2} \left\langle \tilde{\mathbf{p}} \tilde{\mathbf{E}} \right\rangle \tag{2.4}$$

where the angle brackets denote the time average. The factor of $\frac{1}{2}$ comes from the integration, and is thus not present for a permanent dipole. Equation (2) from [24] may then be used to obtain:

$$U_{\text{dip}} = -\frac{1}{2\epsilon_0 c} \operatorname{Re}(\alpha)\, I(\mathbf{r}) \tag{2.5}$$

where $I(\mathbf{r}) = 2\epsilon_0 c |\tilde{E_0}(\mathbf{r})|^2$ is the field intensity[1].

[1]This expression and the corresponding Equation 2.5 comes from equation (2) of [24] In other literatures (e.g. [23]), the intensity of an electromagnetic wave is often written as $I = \frac{1}{2}\epsilon_0 c |\tilde{E_0}|^2$, where the factor $\frac{1}{2}$ comes from the time average of a $\sin^2$ function. The use of Equation 2.5 leads to results that are corroborated by at least one paper [25] and is hence left as such and used consistently throughout this thesis. Whether the expression is physically correct is out of the scope of this thesis.

As the nature of this potential is conservative, the force is defined via $F_{\text{dip}}(\mathbf{r}) = -\boldsymbol{\nabla} U_{\text{dip}}(\mathbf{r})$. As such, the minima of the dipole potential U_{dip} may be used to trap the atom.

Using the aforementioned harmonic oscillator model, the polarisability $\tilde{\alpha}$ can be calculated [24]. In this case, the driving force is provided by the oscillating electric field $\tilde{\mathbf{E}}$, whereas the damping Γ_ω occurs as a result of radiative energy loss (spontaneous decay):

$$\ddot{x} + \Gamma_\omega \dot{x} + \omega_0^2 x = -\frac{q_e}{m_e}|\tilde{\mathbf{E}}(t)| \tag{2.6}$$

Here, ω_0 is the frequency of the transition (for ^{6}Li: $\omega_0 = 2\pi \cdot c/671\,\text{nm}$), and Γ_ω is given by [24]:

$$\Gamma_\omega = \frac{q_e^2 \omega^2}{6\pi\epsilon_0 m_e c^3} \qquad \Leftrightarrow \qquad \frac{q_e^2}{m_e} = \frac{6\pi\epsilon_0 c^3}{\omega^2}\Gamma_\omega \tag{2.7}$$

Solving this differential equation for $\tilde{\alpha}(\omega)$:

$$\tilde{\alpha}(\omega) = \frac{q_e^2}{m_e}\frac{1}{\omega_0^2 - \omega^2 - i\omega\Gamma_\omega} \tag{2.8}$$

The damping factor Γ_ω is then rewritten as a function of the on-resonance damping such that $\Gamma_\omega = \left({}^{\omega}/_{\omega_0}\right)^2 \Gamma_{\omega_0}$. The expression (2.7) can then be substituted into (2.8) to obtain equation (8) of [24]:

$$\tilde{\alpha} = \frac{6\pi\epsilon_0 c^3}{\omega_0^2}\frac{\Gamma_{\omega_0}}{\omega_0^2 - \omega^2 - i\left(\frac{\omega^3}{\omega_0^2}\right)\Gamma_{\omega_0}} \tag{2.9}$$

Here, Γ_{ω_0} is the natural linewidth of the transition and is given by $(2\pi \cdot 5.872\,\text{MHz})$ for ^{6}Li. [26]

At large detunings and negligible saturation, we may deduce the following from equation (2.9):

- If the trap is red-detuned (i.e. $\omega < \omega_0$), then $(\omega_0^2 - \omega^2) > 0$, and $\text{Re}(\tilde{\alpha})$ is positive, leading to a negative dipole potential that attracts atoms into light field, acting as wells.
- If the trap is blue-detuned (i.e. $\omega > \omega_0$), then $(\omega_0^2 - \omega^2) < 0$, and $\text{Re}(\tilde{\alpha})$ is negative, leading to a positive dipole potential that repels atoms out of the light field, acting as walls.

For the ODT designed in this thesis, infrared laser light at 1070 nm is to be used. Compared to the wavelength of light resonant with the transition of ^{6}Li at 671 nm, the laser light is red-detuned. The ODT is thus an attractive dipole trap.

The *trap depth* is then given by the deepest point of the potential, while the *trap frequency* is obtained through a harmonic approximation[2] of the potential around the deepest point. The trap frequency characterises the natural frequency of the oscillation around the potential minimum and differs for different trap geometries.

[2] For analytical trap potentials, one may choose to do a second order Taylor expansion. For arbitrary potential shapes, a quadratic fit through the plane of interest would be more optimal. For some potential shapes (e.g. flat-bottomed), a harmonic approximation is not reasonable. For these trap shapes, no meaningful trap frequencies exist.

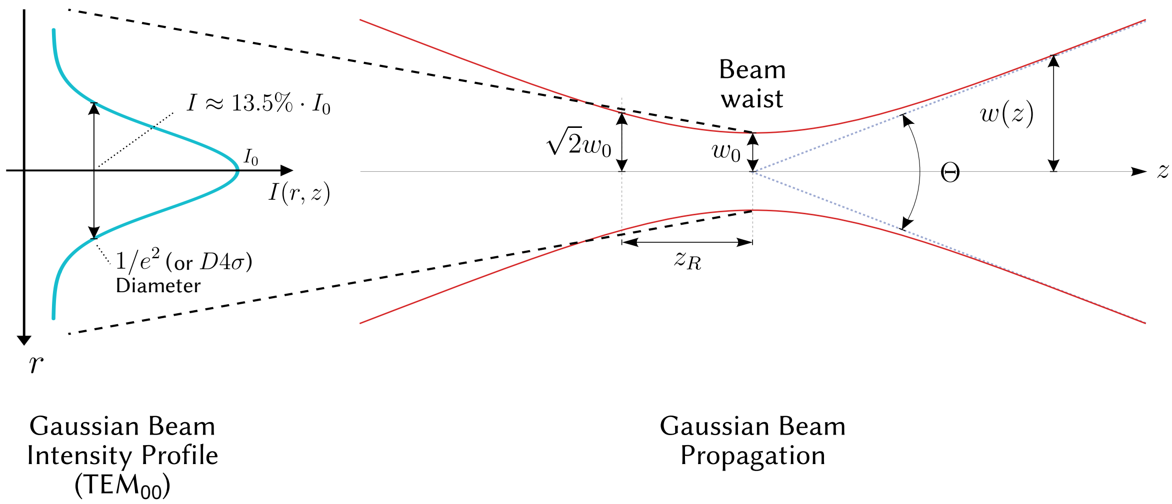

Figure 2.1: Illustration of the Gaussian beam profile and its propagation. In the diagram, $I(r, z)$ is the intensity of the laser beam as a function of the horizontal position z and radial position r, while $w(z)$ refers to the beam radius as a function of z. The divergence angle of the beam is indicated with Θ, and z_R is the Rayleigh length. Illustration adapted from [27].

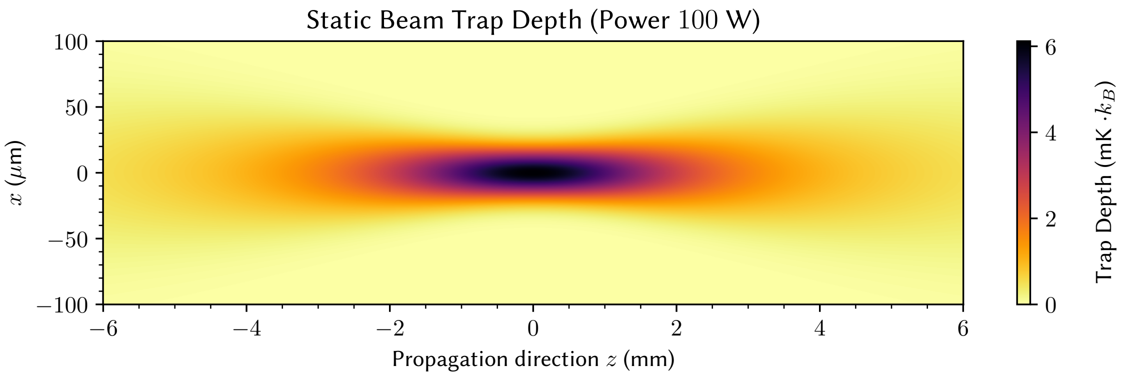

Figure 2.2: Calculated trap depth for a 1070 nm static, single-beam dipole trap using a Gaussian beam with a power of $P = 100\,\mathrm{W}$, a beam waist of $w_0 = 25\,\mu\mathrm{m}$, centred at $z_0 = 0\,\mathrm{mm}$.

2.1.2 The Gaussian Beam

The Gaussian beam gets its name from the transverse profile of its optical intensity, which can be described with a Gaussian function (Figure 2.1, left). Many laser sources, including the lasers used in this thesis, have such a transverse beam profile[3]. For a Gaussian beam with power P, its intensity profile can be described with:

$$I(r,z) = \frac{2P}{\pi w(z)^2} \exp\left(-2\frac{r^2}{w(z)^2}\right) \tag{2.10}$$

where $w(z)$ is the radius of the beam[4] at position z. Since the Gaussian profile extends to infinity, this radius is defined as the distance from the beam axis where the intensity drops to $1/e^2 \approx 13.5\,\%$ of the maximum value [29]. This is also known as the $1/e^2$ radius.

In some cases, the $D4\sigma$ radius is to be used [30]. For Gaussian beams, the $D4\sigma$ radius coincides with the $1/e^2$ radius [31].

In a situation where there is astigmatism, as is the case in our experiments, then $z_{0,x} \neq z_{0,y}$ and $w_x \neq w_y$. The intensity profile is thus elliptical and may be described with the product of two one-dimensional Gaussian profiles:

$$I(x,y,z) = \frac{2P}{\pi w_x(z) w_y(z)} \exp\left\{-2\left[\left(\frac{x}{w_x(z)}\right)^2 + \left(\frac{y}{w_y(z)}\right)^2\right]\right\} \tag{2.11}$$

For each axis of such a Gaussian beam, its propagation may be described with the following equation:

$$w(z) = w_0\sqrt{1+\left(\frac{z-z_0}{z_R}\right)^2} = w_0\sqrt{1+(z-z_0)^2\left(\frac{M^2\lambda}{\pi w_0^2}\right)^2} \tag{2.12}$$

with the Rayleigh length $z_R = \frac{\pi w_0^2}{M^2\lambda}$.

The Rayleigh length is the distance from the beam waist in the propagation direction at which point the beam radius is increased by a factor $\sqrt{2}$. It is a measure of how far the beam can propagate without diverging significantly [32].

An illustration of the propagation of a Gaussian beam is depicted in Figure 2.1.

For a single, focused-beam (TEM_{00}) ODT, the Equations 2.10 and 2.12 describe the intensity distribution at every point in space, thus determining the geometry of the trap. Given a trap

[3]More sophisticated analyses of laser beam profiles exist, such as in [28]. In this thesis, only the simplest model of a Gaussian beam is used.

[4]Not to be confused with the ω from the previous section, which represents the angular frequency of the incident light.

depth U_0, the trap frequencies for a non-astigmatic laser beam are therefore given by [33]:

$$\omega_{\text{trap, radial}} = \sqrt{\frac{4U_0}{mw_0^2}} \qquad \omega_{\text{trap, axial}} = \sqrt{\frac{2U_0}{mz_R^2}} \tag{2.13}$$

The calculated trap depth profile for a single-beam dipole trap created with a Gaussian beam is depicted in Figure 2.2.

2.2 Time-Averaged Potentials

Colloquially often known as a "sweeping" or "painting" trap, a time-averaged ODT uses a laser beam whose position is spatially modulated to create a time-averaged intensity distribution, which results in a time-averaged dipole potential that can be used to trap the atoms [34].

The form of the modulation then determines the shape of the dipole potential experienced by the atom. With the modulation being fully controllable, this allows a time-averaged ODT to have arbitrary trap geometries that can be rapidly and dynamically changed.

Such a time-averaged ODT could, for example, be used to achieve a large initial trapping volume, which can then be reduced during the process of evaporative cooling to increase the density of the atoms. This increases the scattering within the atom cloud, leading to faster thermalisation during the cooling process that reduces the total time required to cool atoms to a degenerate quantum gas [35].

Since evaporative cooling is often the longest step within a cycle of a fermionic quantum gas microscope, accelerating this promises to significantly reduce cycle times in the final experiment.

2.2.1 Mathematical Formalism and Numerical Methods

Given a modulation amplitude A, a modulation frequency $f_{\text{mod}} = {}^1/_{\tau_{\text{mod}}}$ and an arbitrary modulation function $f(t)\colon [0,1] \mapsto [-1,1]$, the potential $U(x,y,z,t)$ at any point in space (x,y,z) and time fraction $t = \frac{\text{real time}}{\tau_{\text{mod}}}$ of the modulation period τ_{mod} may be derived from equation (2.5):

$$U(x,y,z,t) = -\frac{\text{Re}(\alpha)}{2\epsilon_0 c} I\Big(x - Af(t)\,, y, z\Big) \quad \text{where} \quad t \in [0,1] \tag{2.14}$$

where x is the axis in which the beam is being modulated, and $I(x,y,z)$ is the function describing the intensity of the static, non-modulated beam. Since $f(t)$ is independent of τ_{mod}, This equation is independent of the modulation frequency, which is not necessarily the case experimentally.

The time-averaged potential $\bar{U}(x,y,z)$ may then be described as such:

$$\bar{U}(x,y,z) = \int_0^1 U(x,y,z,t)\,\mathrm{d}t = -\frac{\text{Re}(\alpha)}{2\epsilon_0 c}\int_0^1 I\Big(x - Af(t)\,, y, z\Big)\,\mathrm{d}t \tag{2.15}$$

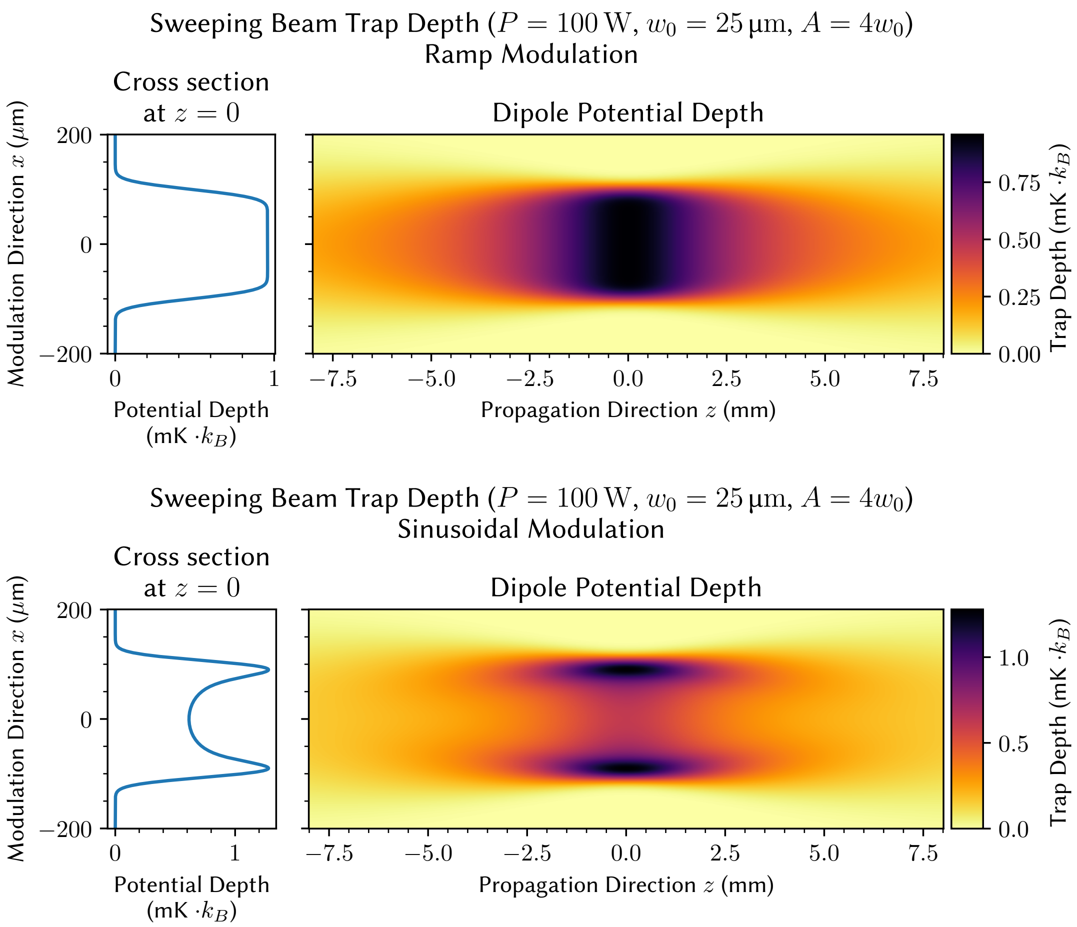

Figure 2.3: Trap geometry visualisation of a 1070 nm single-beam time-averaged dipole trap with different modulation functions obtained through numerical integration. The beam simulated is a Gaussian beam centred around $z_0 = 0$ mm with power $P = 100$ W, beam waist $w_0 = 25$ μm and modulation amplitude $A = 4w_0$. For a ramp function (top), we see that the trap is flat-bottomed and is thus anharmonic.

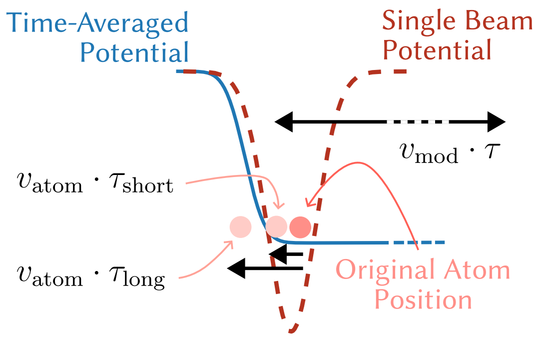

Figure 2.4: Snapshot of a sweeping beam and a ^{6}Li atom in a flat-bottomed time-averaged potential. If the period of the modulation $\tau = \tau_{\text{short}}$, then the atom would not have drifted far and would be recaptured. If $\tau = \tau_{\text{long}}$, then the atom would have drifted too far and will be lost.

Examples of the modulation function $f(t)$ include a ramp modulation $f_{\text{ramp}}(t) = 2\left(t - \frac{1}{2}\right)$ and a sinusoidal modulation $f_{\text{sine}}(t) = \sin(2\pi \cdot t)$.

As the analytical solution to the integral may not always be readily available, the final shape of the time-averaged potential may also be simulated using standard numerical integration methods [36] as depicted in Figure 2.3.

In order to construct arbitrary potential shapes, one may choose to use the methods described in [37].

2.2.2 Modulation Frequency

One important factor that impacts the effectiveness of the time-averaged ODT is its modulation frequency $\omega_{\text{mod}} = 2\pi f_{\text{mod}}$.

If the modulation is very slow, then the trapped atoms will notice the change in the position of the potential minimum and follow the position modulation of the laser beam. This is similar to the concept behind optical tweezers.

If the modulation is fast enough, then the atoms will only experience the local average of the light intensity. Since the dipole potential is proportional to the intensity of the light field (see Equation 2.5), a time-averaged dipole potential will be created.

In order to be in the latter regime, it is commonly stated that the modulation frequency ω_{mod} needs to be much larger than the trap frequency ω_{trap} [34]. However, since the final time-averaged trap is likely anharmonic in shape (e.g. a flat-bottomed trap, as we saw in Figure 2.3), there is no meaningful trap frequency defined. Nevertheless, a first-order approximation for the minimum modulation frequency can still be obtained by examining the situation in the classical picture.

Consider an atom in a regime where the the modulation is already fast enough such that the atom experiences a time-averaged potential and is not following the beam's spatial modulation.

Now, further consider that the atom finds itself in the scenario depicted in Figure 2.4, in which it is moving with a velocity v_{atom} to the left at the edge of the time-averaged dipole potential.

Since the position of the laser beam is modulated with a certain period $\tau = {}^1/_{f_{\text{mod}}}$ to create the aforementioned potential, this atom at the edge will only experience the dipole force every period τ. This is the point in time when the position of the laser beam overlaps with the position of the atom again.

If the laser beam returns to the atom fast enough (in $\tau = \tau_{\text{short}}$), then the atom is recaptured. However, if the laser beam only returns after $\tau = \tau_{\text{long}}$, then the atom would have travelled too far out and can no longer be recaptured by the laser beam. This atom would then be lost.

We can thus set a lower bound for the distance $\Delta x_{\text{atom}} = v_{\text{atom}} \cdot \tau$ travelled by the atom in one period of the modulation τ such that the laser beam can no longer recapture the atom:

$$\Delta x_{\text{atom}} > \text{Diameter of the laser beam} = 2w_0 \tag{2.16}$$

The inequality (2.16) may then be reversed to obtain the boundary condition for τ:

$$\Delta x_{\text{atom}} = v_{\text{atom}} \cdot \tau \ll 2w_0 \qquad \Rightarrow \qquad \tau \ll \frac{2w_0}{v_{\text{atom}}} \tag{2.17}$$

Since $\tau = {}^1/_{f_{\text{mod}}}$, the inequality (2.17) may be rewritten as such:

$$f_{\text{mod}} \gg \frac{v_{\text{atom}}}{2w_0} \tag{2.18}$$

If the atom has an energy of U_{atom}, then its thermal velocity v_{atom} is given by:

$$U_{\text{atom}} = \frac{1}{2} m v_{\text{atom}}^2 \qquad \Rightarrow \qquad v_{\text{atom}} = \sqrt{\frac{U_{\text{atom}}}{\frac{1}{2}m}} = \sqrt{\frac{2U_{\text{atom}}}{m}} \tag{2.19}$$

Substituting equation (2.19) into equation (2.18), the limit of f_{mod} as a function of the energy U_{atom} of the atom is obtained:

$$f_{\text{mod}} \gg \frac{\sqrt{\frac{2U_{\text{atom}}}{m}}}{2w_0} \tag{2.20}$$

We would like to trap all atoms that the ODT can theoretically trap if it were infinitely fast and purely limited by the intensity of the light. Hence, instead of considering the average temperature of the atoms in the trap, as is often reported in papers, it is reasonable to simply look at the energy of the most energetic atoms, given by the trap depth $U_0 = U_{\text{atom}} = k_B T_{\text{trap}}$:

$$f_{\text{mod}} \gg \frac{1}{2w_0} \sqrt{\frac{2U_0}{m}} \tag{2.21}$$

This serves as the lower limit of the required modulation frequency f_{mod}.

2.3 Acousto-Optical Modulator (AOM)

An acousto-optic modulator (AOM) is a device that is used to diffract and change the frequency of light going through the device using the acousto-optic effect. Typically, an AOM is made out of a piezo-electric transducer, a crystal, and an absorber, as depicted Figure 2.5. By applying a radio frequency (RF) signal of frequency f_{AOM} to the piezo-electric transducer, sound waves with the same frequency f_{AOM} is produced and sent through the AOM crystal.

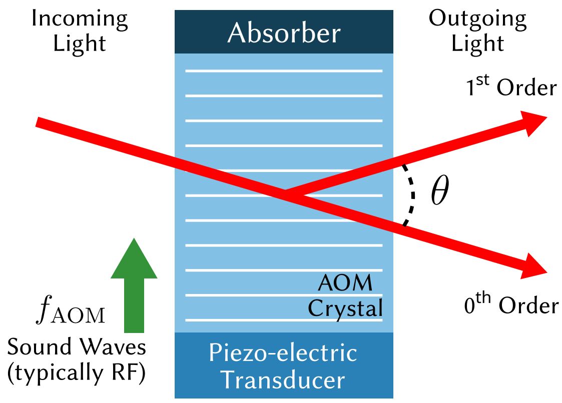

Figure 2.5: Working principle of the acousto-optic modulator (AOM). The incoming beam is diffracted according to the Bragg condition as a function of the frequency f_{AOM} of the radio frequency (RF) signal at the piezo-electric transducer. The diffraction angle θ is exaggerated.

Since these sound waves are typically energetic longitudinal pressure waves, they lead to mechanical strain in the AOM crystal that causes a change in the local refractive index of the crystal. This change in refractive index is periodic and is given by the wavelength of the RF sound waves, creating a travelling refractive index grating which diffracts the light [38]. The process may also be thought of as the result of phonon-photon interactions.

An AOM typically operates in the Bragg regime, where Bragg-refraction occurs. The diffraction angle θ must therefore satisfy the Bragg criterion [39]:

$$2\Lambda \sin\theta = m\frac{\lambda}{n} \tag{2.22}$$

where Λ is the wavelength of the sound wave, m the order of diffraction, λ the wavelength of the light in vacuum and n the refractive of the crystal. This results from the consideration that the angle of incidence of the light should be equal to $\theta_B = {}^{\lambda}/_{2n\Lambda}$, the Bragg angle.

Given the speed of sound $v_{\text{sound}} = f_{\text{AOM}} \cdot \Lambda$ in the crystal, equation (2.22) may then be rewritten as:

$$\sin\theta = \frac{m}{2}\frac{\lambda}{n\Lambda} = \frac{m}{2}\frac{\lambda}{n \cdot v_{\text{sound}}} f_{\text{AOM}} \tag{2.23}$$

For small angles, $\sin\theta \approx \theta$ and θ is approximately linear in f_{AOM}, the driving frequency of the AOM. As a result, we can modulate the angle of deflection θ by modulating the frequency f_{AOM} of the RF signal being applied to the AOM.

However, since an AOM has a finite bandwidth in terms of its diffraction efficiency as a function of the frequency of the input RF signal f_{AOM}, the adjustable range of the angle of deflection θ is also limited[5].

Besides angular modulation, AOMs may be used to modulate the intensity of the transmitted laser light. For these Bragg-type modulators, the intensity of the first order diffracted beam I is given by [38]:

$$\frac{I}{I_0} = \sin^2\left(\frac{\Delta\phi}{2}\right) \tag{2.24}$$

where I_0 is the transmitted intensity without the presence of the acoustic beam, and $\Delta\phi$ is the maximum phase shift given by [38]:

$$\Delta\phi = \frac{2\pi l \Delta n}{\lambda} \tag{2.25}$$

where $\Delta n \propto \sqrt{P_{\text{sound}}}$ is the acoustically produced change in refractive index. Since the power of the sound wave P_{sound} is determined by the power of the RF signal supplied to the piezo-electric transducer, the transmitted intensity in the first order may also be controlled by changing the power of the applied RF signal.

Thus, an AOM may be used to control the angle of deflection θ and the intensity I of the light in the first order.

[5] Refer to Appendix A for an example of an AOM diffraction efficiency curve.

Chapter 3

Design and Planning

The goal of the optical dipole trap (ODT) is the effective loading and efficient evaporative cooling of cold ^{6}Li atoms in the glass cell of the FermiQP machine (see Figure 3.1). This chapter details the various considerations that went into the design of the ODT to fulfil these goals. Some simulations will also be presented to improve our understanding of the designed trap.

3.1 Working Principle and Optical Setup

One of the main challenges of loading an ODT from a 3D magneto-optical trap (MOT) is the low atom density in the 3D MOT and the need for a high density of atoms for efficient evaporative cooling. This is because a high atom density increases the rate of collisions between the atoms, thereby increasing the speed of thermalisation, which in turn means that the evaporative cooling can happen at a faster rate [35].

In other words, the trap needs to be large to capture as many atoms as possible from the low density atom cloud in the 3D MOT, but once loaded, be small to increase the density of the atom cloud.

To overcome this challenge, a solution is proposed in which a tightly focused laser beam is to be spatially modulated to create a time-averaged or "sweeping" ODT [34]. With a small static beam waist, a large sweeping range may be used initially during the loading process to load a large number atoms from the 3D MOT. The trap size can then be reduced dynamically during the evaporative cooling process to increase the density of the atoms and provide a tight confinement at the very end.

The proposed spatial modulation of the focused laser beam may be realised by an optical setup consisting of an acousto-optic modulator (AOM) and a three-lens system as depicted in Figure 3.2.

Consider the optical setup depicted in Figure 3.2a. In this first half of the setup, a collimated beam is passed through an acousto-optic modulator (AOM) placed at position A. Depending on the driving frequency of the AOM, the first order beam will be deflected by an angle α away from

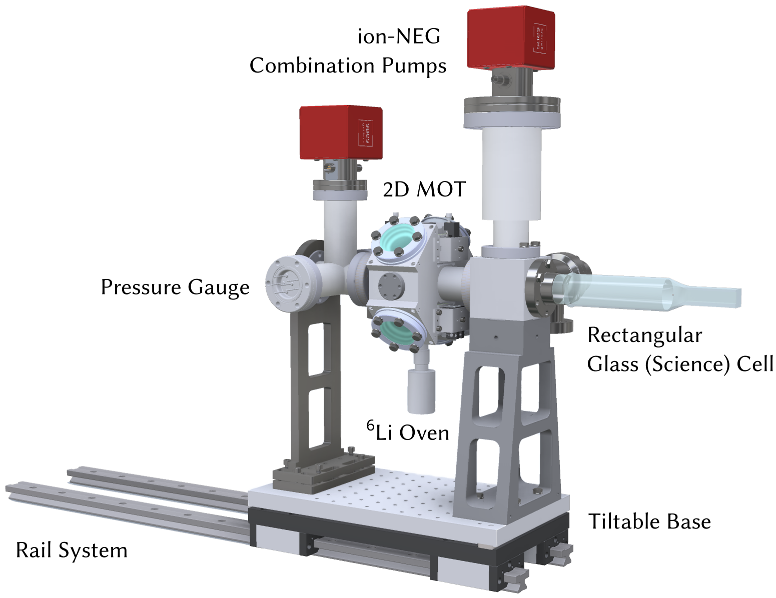

Figure 3.1: Current design of the FermiQP vacuum chamber, including the science cell [41]. The optics of the proposed optical dipole trap (ODT) will go around the glass cell.

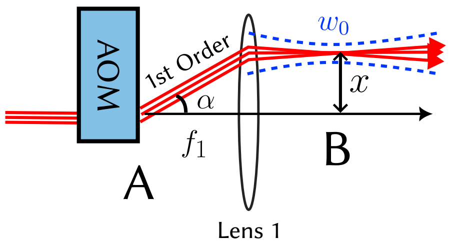

(a) With alignment of the 0$^{\text{th}}$ order beam with the principal axis. Angle α exaggerated.

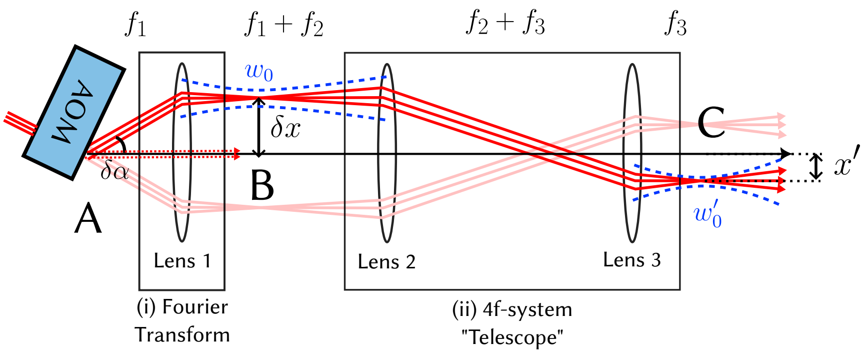

(b) With alignment of the 1$^{\text{st}}$ order beam at $f_{\text{AOM, cent}}$ with the principal axis. Angles exaggerated.

Figure 3.2: Sketch for an optical system used for (i) transforming a deflection angle from an AOM positioned at A into a displacement in the intermediate imaging plane B perpendicular to the principal axis, and (ii) shrinking the beam waist to the desired beam waist at the ^{6}Li atoms positioned at C. The sketch shows an exaggerated fixed angle $\delta\alpha$, which will then be varied to move the beam.

the optical axis. Since the AOM is positioned at the focal length f_1 away from biconvex lens 1, this angular displacement is transformed into a parallel displacement x away from the principal axis in the intermediate imaging plane B. Since the beam is simply displaced while remaining parallel to the principal axis, the corresponding beam waist w_0 does not change. Thus, by dynamically changing the driving frequency of the AOM, we can change the displacement of the beam from the principal axis [40].

The aim of the next few paragraphs is to derive the expression for the displacement $\mathrm{d}x'$ per change in angle $\mathrm{d}\delta\alpha$ at the AOM using the aforementioned three-lens optical setup. This will allow us to understand what the maximum spatial modulation $\Delta x'$ in the plane of the atoms would be.

An AOM typically has a diffraction efficiency[1] that is convex as a function of the driving frequency f_{AOM}, with its peak at a central driving frequency $f_{\text{AOM, cent}}$ and a bandwidth of Δf_{AOM}. As a result, the beam can be deflected by an angle from $\alpha = \alpha_{\text{cent}} - \delta\alpha_{\text{max}}$ to $\alpha = \alpha_{\text{cent}} + \delta\alpha_{\text{max}}$, where α_{max} is determined by Δf_{AOM}.

Trigonometric considerations lead to the following conclusions: at $f_{\text{AOM}} = f_{\text{AOM, cent}}$, the angle of deflection α_{cent} is given by:

$$\tan\alpha_{\text{cent}} = \frac{x_{\text{cent}}}{f_1} \quad \Rightarrow \quad x_{\text{cent}} = f_1 \tan\alpha_{\text{cent}} \tag{3.1}$$

Since the angle of deflection from an AOM is typically small (around $1°$) [42], the approximation $\tan\theta \approx \theta$ may be used, obtaining:

$$x_{\text{max}} = f_1 \tan\left(\alpha_{\text{cent}} + \delta\alpha_{\text{max}}\right) \approx x_{\text{cent}} + \left(f_1 \cdot \delta\alpha_{\text{max}}\right) = x_{\text{cent}} + \left(\delta x_{\text{max}}\right) \tag{3.2}$$
$$x_{\text{min}} = f_1 \tan\left(\alpha_{\text{cent}} - \delta\alpha_{\text{max}}\right) \approx x_{\text{cent}} - \left(f_1 \cdot \delta\alpha_{\text{max}}\right) = x_{\text{cent}} - \left(\delta x_{\text{max}}\right) \tag{3.3}$$

We now align the deflected first order beam at the central driving frequency of our AOM with the principal axis of the lens system. The beam in the plane B may now be modulated with a range of $\Delta x = 2\delta x = 2f_1 \cdot \delta\alpha_{\text{max}}$, dictated by the diffraction efficiency of the AOM. This optical setup is depicted in Figure 3.2b.

The intermediate imaging plane B is then imaged through the $4f$-system onto the image plane C, where the ^{6}Li atoms will be situated. In the image plane C, the displacement δx and beam waist w_0 has now been scaled by the magnification factor given by $\mathcal{M} = f_3/f_2$ to give

$$x' = \mathcal{M} \cdot \delta x \qquad \text{and} \qquad w_0' = \mathcal{M} \cdot w_0 \tag{3.4}$$

respectively, where f_i is the focal length of the ith lens. This then results in a sweeping range in the plane of the atoms C of:

$$\Delta x' = \mathcal{M}\left(2f_1 \cdot \delta\alpha_{\text{max}}\right) = \frac{f_1 f_3}{f_2} \cdot 2\delta\alpha_{\text{max}} \tag{3.5}$$

The change in deviation $\mathrm{d}x'$ per change in angle $\mathrm{d}\left(\delta\alpha\right)$ may also be calculated similarly:

$$\mathrm{d}x' = \frac{f_1 f_3}{f_2}\,\mathrm{d}\left(\delta\alpha\right) \tag{3.6}$$

[1] See Appendix A for more information about the diffraction efficiency of the AOM used in this thesis.

3.2 Considerations and Project Requirements

3.2.1 Trap Depth and Geometrical Considerations

The ODT for the final setup shall be realized with a 200 W diode-pumped spatially single-mode, spectrally multi-mode, linearly polarized continuous wave (CW) Ytterbium fibre laser (YLR-200-LP-WC manufactured by IPG Photonics, henceforth *IPG laser*). With a wavelength λ of 1070 nm [43], the laser is far red-detuned from the 671 nm transition of ^{6}Li [26], allowing it to create an attractive potential proportional to the light intensity (see section 2.1).

A laser power of 100 W is planned, pending experimental optimization with the actual trapping and cooling procedure once the other parts of the experiment are ready.

The expected temperature of the ^{6}Li atoms to be loaded into the ODT plays a decisive role in the trap depth required. The proposed ODT will be used to load the atoms from the 3D MOT into the optical lattice. Before the loading occurs, gray molasses, a method of sub-Doppler laser cooling, will be employed, after which the ^{6}Li atoms is expected to cool down from a few hundred microkelvins to approximately 50 μK [15].

Due to the thermal distribution of the atoms in the trap, the thermal energy of the atoms trapped in an ODT is approximately 10 % of the trap depth [44]. Thus, the ODT needs a trap depth of at least 10 times deeper than that of the energy associated with the temperature of the atoms. Therefore, the trap depth has to be at least $U_0 = 0.5\,\mathrm{mK} \cdot k_B$ and could possibly need to be as deep as a few millikelvins $\cdot\, k_B$.

Due to spatial constraints of the experimental setup, the laser beam will be focused onto the atoms with a lens of focal length $f = 0.2\,\mathrm{m} = 200\,\mathrm{mm}$. Considering the final confinement of the atoms, a beam waist of 25 μm in the image plane C is targeted.

3.2.2 Modulation Frequency

The modulation frequency is also of high importance. Instead of following the modulation, the time-averaged trap requires that the atoms only experience the time-average of the modulated potential.

As previously discussed in subsection 3.2.1, the trap depth on the order of a few millikelvins $\cdot\, k_B$ is targeted. Depending on the configuration of the ODT, such as the sweeping range and laser power, this can vary. As a rule of thumb, the larger the sweeping range, the more spread out the intensity distribution, and thus the shallower the trap depth. In this case, it is reasonable to assume a trap depth of $5\,\mathrm{mK} \cdot k_B$ for calculation purposes. The limit may then be calculated from Equation 2.21 using the values $m_{^6\mathrm{Li}} = 6.015\mathrm{u} = 9.988 \times 10^{-27}$ kg [26] and $w_0 = 25$ μm:

$$f_{\mathrm{mod}} \gg 7.44 \times 10^4\,\mathrm{Hz} \tag{3.7}$$

Thus, the modulation frequency f_{mod} should at least be on the order of 10^5 Hz. To have some flexibility and tuning range, a setup that can achieve a modulation frequency of 10^6 Hz would be more optimal. Should the high modulation frequency turn out to be unnecessary, it can be turned down again.

A modulation frequency of 1 MHz is therefore targeted in this thesis.

3.2.3 Crossed-Beam Dipole Trap

A crossed-beam ODT offers many benefits over a single-beam ODT. By having two nearly counter-propagating laser beams under an angle θ, it allows the trapping potential to be localised to a much smaller area, while providing double the trap depth by doubling the intensity of light at the point of intersection.

Recycling the laser power from the first beam that otherwise would have been dumped, we can double the trap depth without using any additional laser power.

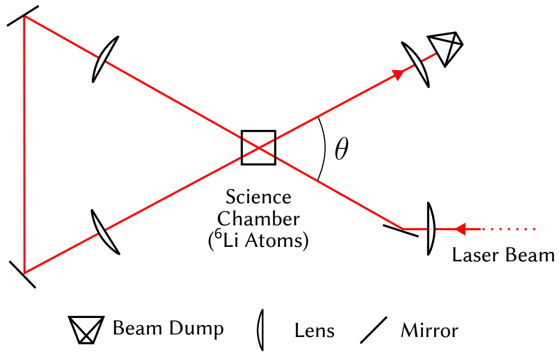

Figure 3.3: Schematics for a crossed-beam ODT. Angles exaggerated.

Therefore, it is proposed that the laser beam be folded back on itself in a "bow-tie" format, as depicted in Figure 3.3, to create a crossed ODT.

The IPG laser has a spectral bandwidth of 3.7 nm [45]. This relatively large bandwidth results in a relatively short coherence time ($\Delta\nu_{\text{FWHM}} \propto {}^{1}/_{\tau_c}$) [46] and coherence length. In this case, the coherence length for the IPG laser is on the order of 10 cm. Thus, it is not expected that the crossed-beams will interfere with each other. The resulting light intensity from a crossed ODT is subsequently the sum of the intensities of each beam at each point. See Figure 3.4 for a visualisation of the trap depth of a static crossed ODT.

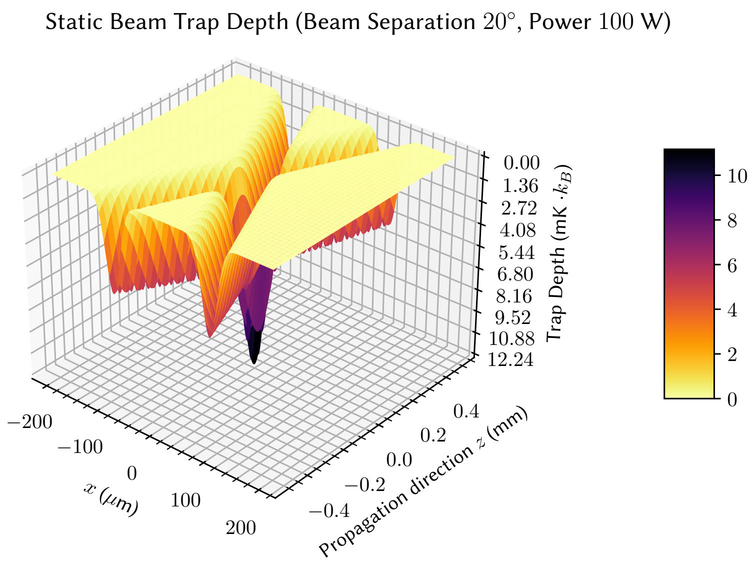

Figure 3.4: 3D visualisation at $\theta = 20°$ beam separation. Two beams of power $P = 100$ W, beam waist $w_0 = 25$ µm, beam quality factor $M^2 = 1.1$, centred at $z_0 = 0$ mm were used. For ^{6}Li, this gives a trap depth of 12.24 mK$\cdot k_B$ at the centre.

3.3 Selection of Parameters

In order to build the optical setup and achieve the desired final beam waist w_0', the correct combination of lenses must be selected. Given an input beam radius of r and the lens setup described in Figure 3.2b, the beam waist w_0 at the intermediate imaging plane B may be calculated by rearranging the Gaussian beam propagation equation (2.12):

$$w_0 = \frac{M^2 \lambda f_1}{\pi r} \tag{3.8}$$

From equation (3.4), the final beam waist w_0' may then be calculated:

$$w_0' = w_0 \left(\frac{f_3}{f_2}\right) = \frac{M^2\lambda}{\pi r} f_1 \left(\frac{f_3}{f_2}\right) = \left(\frac{M^2\lambda}{\pi r} f_3\right) \left(\frac{f_1}{f_2}\right) \tag{3.9}$$

Since $f_3 = 200\,\mathrm{mm}$ is fixed, the correct f_1 and f_2 need to be chosen. The ratio f_1/f_2 may then be obtained by solving equation (3.9):

$$\frac{f_1}{f_2} = \frac{\pi r w_0'}{M^2 \lambda f_3} \tag{3.10}$$

In the above equation, $w_0' = 25\,\mathrm{\mu m}$, $M^2 = 1$, $\lambda = 1070\,\mathrm{nm}$ and $f_3 = 200\,\mathrm{mm}$. The input beam radius r is chosen to be $0.5\,\mathrm{mm}$ to suit the aperture of the AOM.

The results of the calculation for various standard focal lengths f_1 can be found in Table 3.1. From the results, the lens pair, $f_1 = 75\,\mathrm{mm}$ and $f_2 \approx 400\,\mathrm{mm}$, was chosen. However, although lenses with a focal length of $400\,\mathrm{mm}$ do exist, they were unavailable during the period of this thesis. As a result, the next-available lens, a lens with $f_2 = 500\,\mathrm{mm}$ was chosen instead so that the theoretical final beam waist w_0' would be smaller than the planned final beam waist.

f_1/mm	f_2/mm
50	272.47
75	408.71
100	544.95
125	681.18
150	817.42
200	1089.89

Table 3.1: Lens selection calculations for an input beam radius $r = 0.5\,\mathrm{mm}$, $M^2 = 1$, $\lambda = 1070\,\mathrm{nm}$ and $f_3 = 200\,\mathrm{mm}$ such that the final beam radius $w_0' = 25\,\mathrm{\mu m}$.

Experimentally, it is more likely for the beam waist to be bigger rather than smaller than the theoretically calculated one. For example, this could be the result of a less-than-ideal M^2, or misaligned lenses that lead to astigmatism. Thus, a smaller theoretical final beam waist also provides room for experimental errors.

With this set of lenses, a beam waist $w_0' = 20.44\,\mathrm{\mu m}$ was expected.

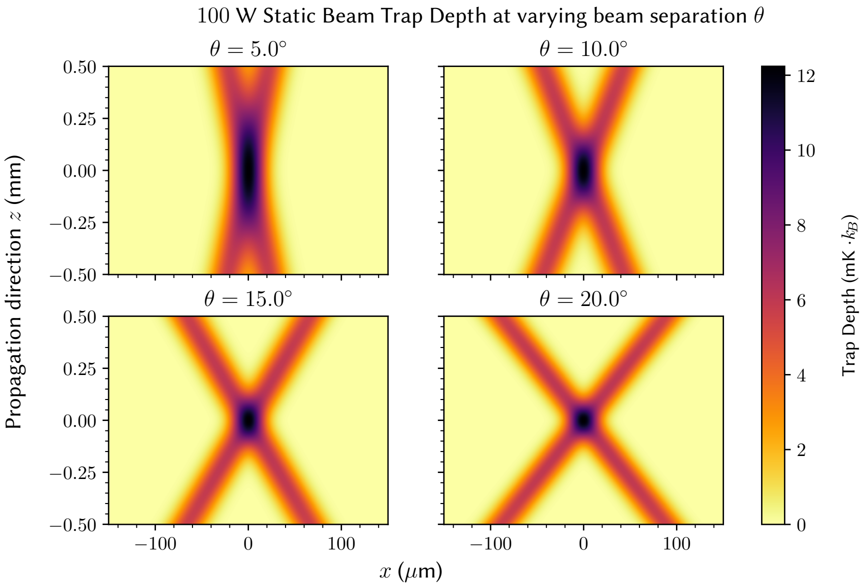

Figure 3.5: 2D pseudocolour visualisation at various beam separation angles θ. Two beams of power $P = 100\,\mathrm{W}$, beam waist $w_0 = 25\,\mu\mathrm{m}$, beam quality factor $M^2 = 1.1$, centred at $z_0 = 0\,\mathrm{mm}$ were used. Compared to Figure 2.2, the trapping area has been localised to an area at least 10 times smaller. As the angle of separation θ increases, the spatial confinement of the trap also increases, but at the expense of decreasing the volume of trapped atoms. *Note that the x- and z-scales are not the same.*

3.4 Numerical Simulations

In order to get a better understanding of the potential shape of an ODT, the dipole potential of a crossed ODT was simulated in Python, based on the different considerations outlined in the previous sections. The results may be seen in Figures 3.4 and 3.5.

Comparing the simulated results obtained here with the previous single-beam simulation results (Figure 2.2), it can be seen that the trapping volume has been localised significantly (almost 10 times smaller).

For a sweeping ODT, a similar simulation was performed, the results of which may be seen in Figures 3.6 and 3.7. However, instead of varying the angle by which the two crossed beams are separated, the modulation amplitude A was varied. From the simulation results, it can be observed that as the sweeping amplitude increases, the trap depth decreases significantly, while the trapping volume increases significantly.

At a modulation amplitude of $A = 1w_0$, the difference between the two modulation functions were not very big, which is reasonable, given that they should both converge to the same potential when the modulation amplitude approaches zero (left-most panel).

At higher modulation amplitudes, a sinusoidal modulation results in potential “valleys” along the edge of the area where the two beams intersect, compared to the flat-bottomed potential that a ramp modulation provides. For simplicity, a ramp modulation was chosen as the first step for experimental implementation.

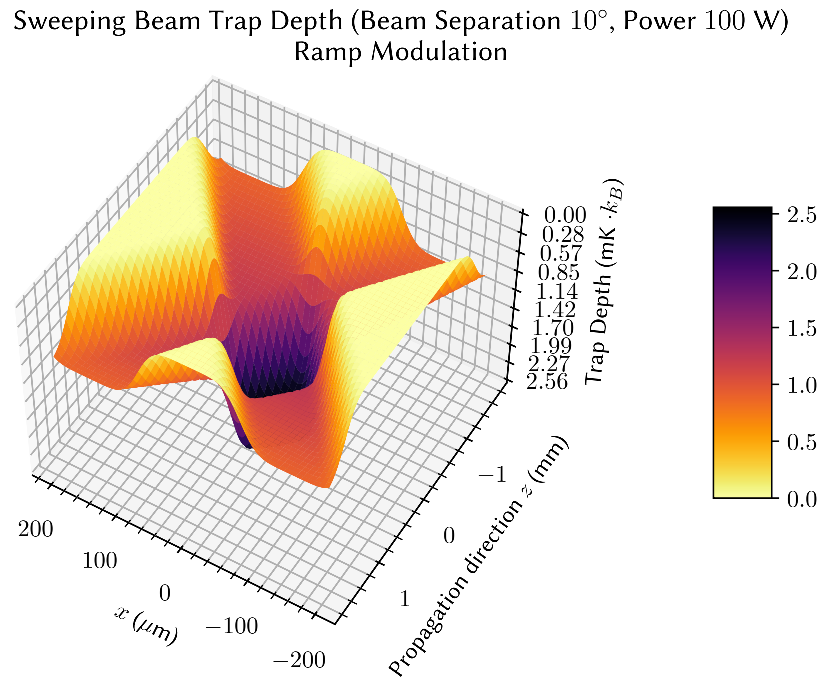

Figure 3.6: 3D visualisation of the time average of a modulated, crossed-beam dipole trap using two beams of power $P = 100\,\mathrm{W}$, beam waist $w_0 = 25\,\mu\mathrm{m}$, beam quality factor $M^2 = 1.1$, centred at $z_0 = 0\,\mathrm{mm}$, modulated at $A = 3w_0$ with a ramp modulation.

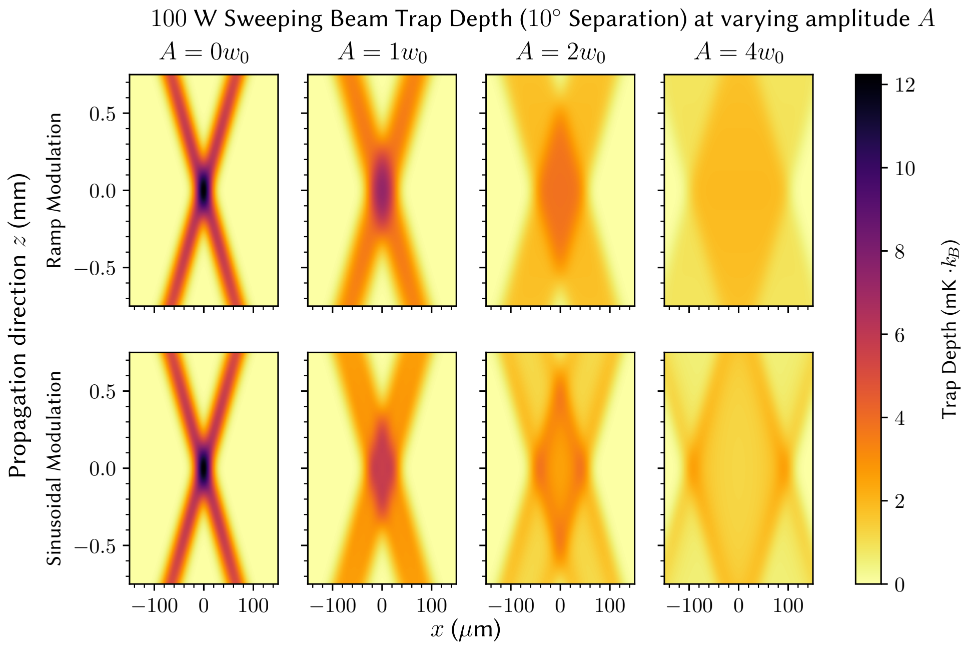

Figure 3.7: 2D visualisation of the one-period time average of a modulated, crossed-beam dipole trap using two beams of power $P = 100\,\mathrm{W}$, beam waist $w_0 = 25\,\mu\mathrm{m}$, beam quality factor $M^2 = 1.1$, centred at $z_0 = 0\,\mathrm{mm}$. Compared to a non-sweeping ODT, the trap depth at $A = 4w_0$ is more than 6 times shallower.

Chapter 4

Experimental Realisation

In this chapter, the experimental realisation of the proposed time-averaged optical dipole trap (ODT) is presented in the form of a proof-of-concept (PoC) setup realised with a lower-power 1064 nm solid-state laser.

Some characterisations of the 200 W YLR-200-LP-WC laser from IPG Photonics (henceforth simply *IPG laser*), along with a way of easily integrating the IPG laser into the PoC setup, will also be presented. This lays the groundwork for the final implementation of the time-averaged ODT with the IPG laser in the FermiQP experiment.

4.1 Proof-of-Concept Setup

To demonstrate the feasibility of the proposed concept for the final ODT of the FermiQP experiment, we use a LCS-T-12 1064 nm continuous wave (CW) diode-pumped solid-state (DPSS) laser from Laser-export Co.Ltd [47] with a TEM_{00} mode as our laser source. The laser light was then attenuated with a $\lambda/2$-waveplate–polarising beamsplitter (PBS) combination[1] and coupled into the setup with a polarisation maintaining (PM) fibre[2]. This setup is depicted in Figure 4.1.

The experimental PoC setup can be seen in Figure 4.2. The beam diameter entering the acousto-optic modulator (AOM) was about 1 mm, which is approximately the aperture of the AOM. Together with the setup in Figure 4.1, two separate stages of attenuation using $\lambda/2$-waveplate–PBS combinations were used.

The attenuation was separated into two stages so that at most 95 % of the incoming light was discarded at each stage. The reason behind this is that most, if not all, linearly-polarised lasers are

[1] This configuration uses the $\lambda/2$-waveplate to change the polarisation axis of the incoming laser light, thereby changing the proportion of transmitted vs. reflected light at the polarising beamsplitter (PBS).

[2] OZ Optic PMJ-3A3A-980-6/125-3-5-1: Standard doped core PM fibre, Angled FC/PC ↔ Angled FC/PC, supports wavelength 980 nm - 1300 nm, 3 mm outer diameter loose tube Kevlar jacket, length 5 m, slow axis of the PM fibre is aligned with respect to the key and locked. [48]

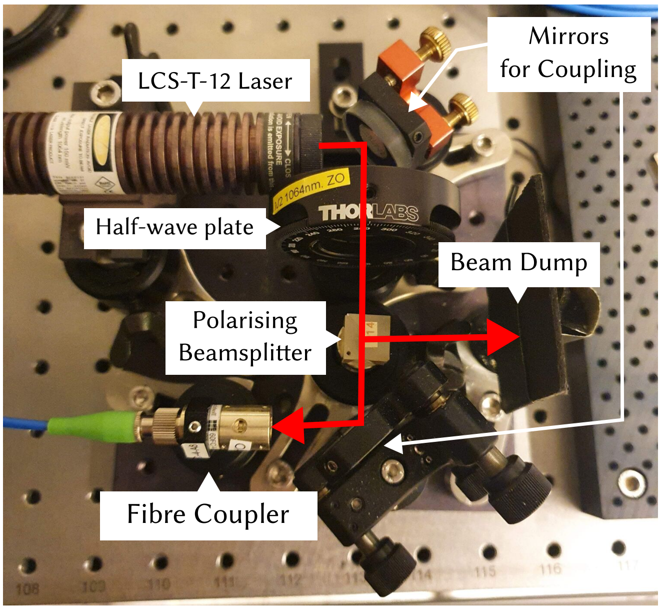

Figure 4.1: LCS-T-12 diode-pumped solid-state (DPSS) laser source setup

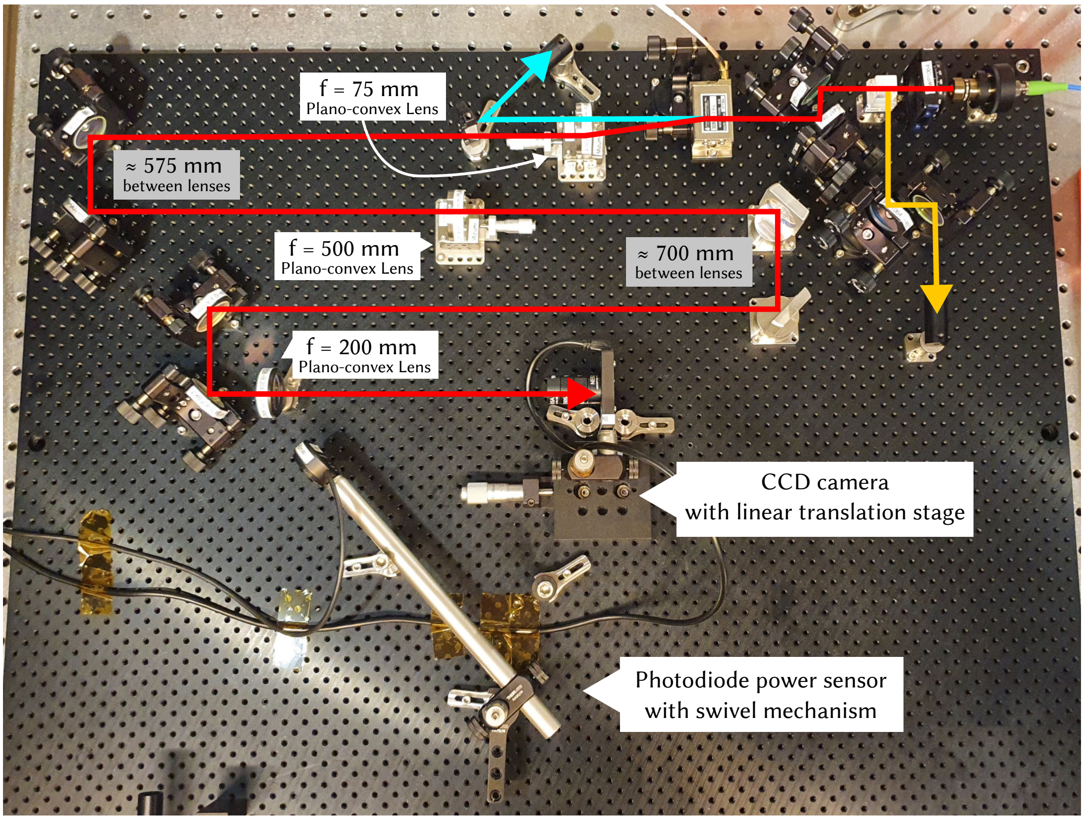

Figure 4.2: Full proof-of-concept (PoC) experimental setup

Location	Power (mW)
Laser output	59.5 ± 0.1
Before the fibre input coupler	4.95 ± 0.10
After the fibre output coupler	2.96 ± 0.10
Before the AOM	0.745 ± 0.010

Table 4.1: Representative powers measured within the setup. Measurements were taken in quick succession to reduce the influence of laser power fluctuations.

designed with a finite extinction ratio[3]. Since the abovementioned method of attenuation discards optical power by means of its polarisation[4], we would only be using the "badly"-polarised light if we chose to discard more than the designed proportion of "well"-polarised light. Consequently, the attenuation was separated into two stages. To provide an intuition on the attenuation stages, a representative measurement of the power at different points within the setup may be found in Table 4.1.

To deflect the beam, we use a 3080-194 AOM from Crystal Technology, Inc.. The AOM was specified to operate around the central frequency of $f_{\text{AOM, cent}} = 80\,\text{MHz}$ and has a bandwidth of 10 MHz. With a beam separation of 20.2 mrad at the central frequency, a sweeping range of $\Delta\alpha = 2(1.2625\,\text{mrad}) = 2.525\,\text{mrad}$ was expected[5] [50]. The subsequent optical elements in the setup were then aligned using the first order beam at $f_{\text{AOM, cent}} = 80\,\text{MHz}$. A difference in deflection angle away from the deflected angle at the central frequency θ_{cent} can thus be translated into a lateral displacement in the final focal plane around the center position.

This 80 MHz radio frequency (RF) signal into the AOM was initially provided by an in-house POS-150+ voltage-controlled oscillator (VCO)-based AOM-driver. However, due to performance issues, this was later replaced with a vector signal generator and a RF amplifier.

The lens and $4f$-optical system outlined in Figure 3.2 was implemented according to the considerations in section 3.3 with the following plano-convex lenses[6]. The planar side of the lens was always placed facing away from the collimated light to reduce abberations.

$$f_1 = 75\,\text{mm} \;\blacktriangleright\; f_2 = 500\,\text{mm} \;\blacktriangleright\; f_3 = 200\,\text{mm}$$

An in-house charge-coupled device (CCD) camera was then used to evaluate the profile of the laser beam at the planned location of the ^{6}Li atoms (Figure 4.4) by taking beam profile measurements at different z-positions along the propagation axis using a micrometer linear translation stage.

[3]LCS-T-12 DPSS laser: $\geq 100:1$ [47] (1 % secondary polarisation); IPG laser: measured $15.4\,\text{dB} \approx 33:1$ at full power (3 % secondary polarisation)

[4]One polarisation-independent method of attenuating infrared (IR) laser power is the use of metal grid attenuators. [49]

[5]Refer to Appendix A for concrete measurements.

[6]Refer to Appendix D for more information on the lenses used.

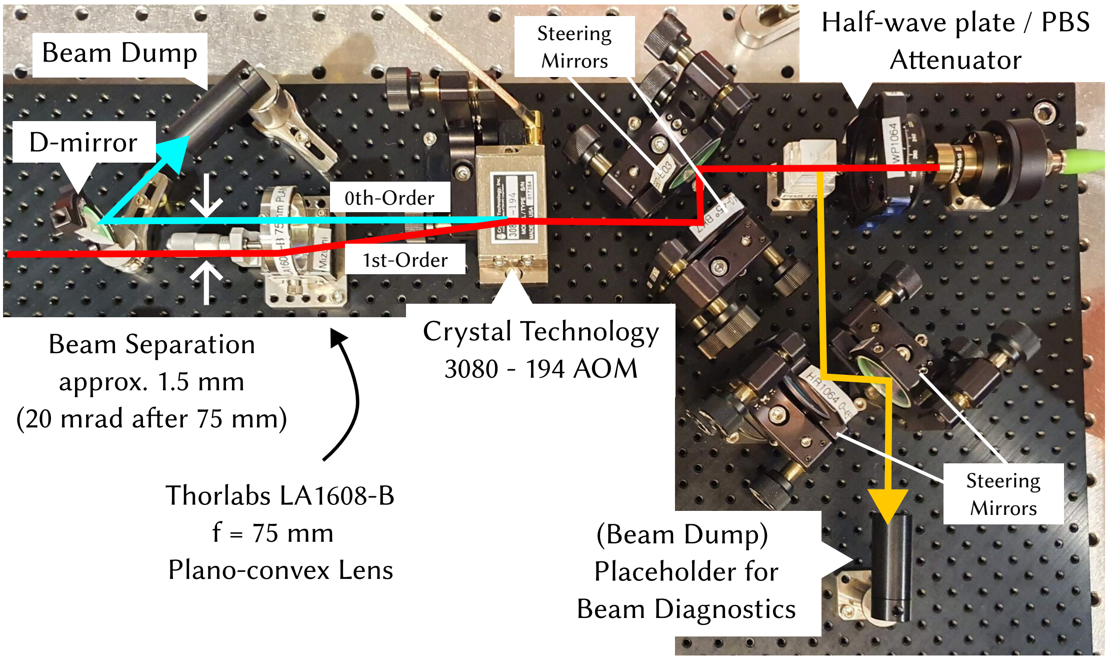

Figure 4.3: Close-up on the first part of the experimental setup. The depicted beam separation is exaggerated for illustration purposes.

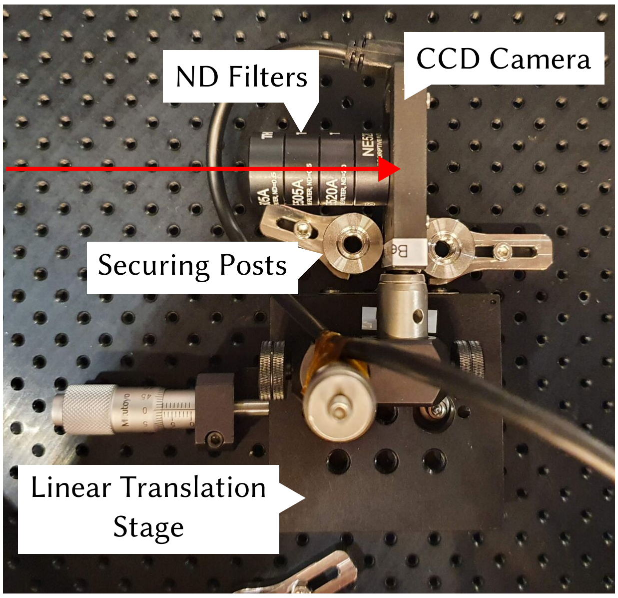

Figure 4.4: Close-up on the CCD camera. The USB-Cable is taped to the post to prevent the transfer of movement on the cable to the camera. For stationary measurements, securing posts were also used to fix the tilt and position of the camera between measurements. To further attenuate the light before it reaches the CCD, neutral-density (ND) filters were used.

A photodiode power sensor was also mounted on a swivel mechanism to facilitate fast switching between beam profile measurements and power measurements (Figure 4.2, bottom).

The optical power directly after the output of the laser was measured to be (61.1 ± 1.5) mW. This corresponds to a percentage error of 2.5 %, much larger than the $< 2\,\%$ power stability as specified by the manufacturer [47]. These power fluctuations were observed to have a period of approximately 5 minutes. To ensure that any power measurements were comparable with any other power measurement, most power measurements were taken over a timespan of approximately 5 minutes. In other cases, the measurements were taken in quick succession so that the fluctuations would have negligible effects on the values obtained.

As it was not possible to image a crossed-beam ODT setup with a beamprofiler or powermeter, only a single beam was characterized in the PoC setup. From the understanding of a single-beam ODT, it is reasonable to assume similar parameters will also apply to the reflected beam.

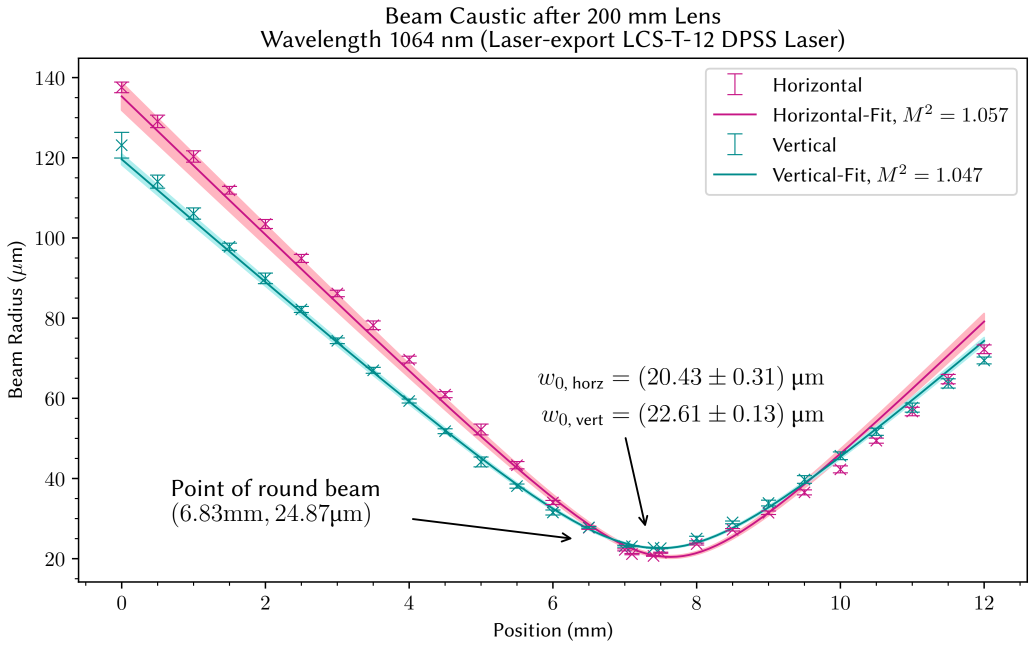

Figure 4.5: Beam caustic measurement after the final 200 mm Lens. Shaded area represents confidence interval. An astigmatism of (0.15 ± 0.05) mm was observed, which was likely caused by the inaccurate placement of the lens.

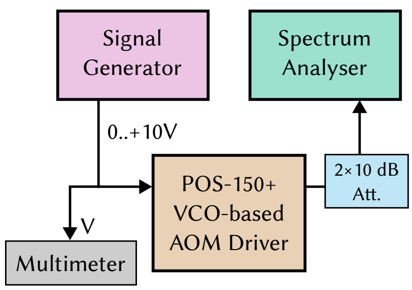

(a) Measurement schematics

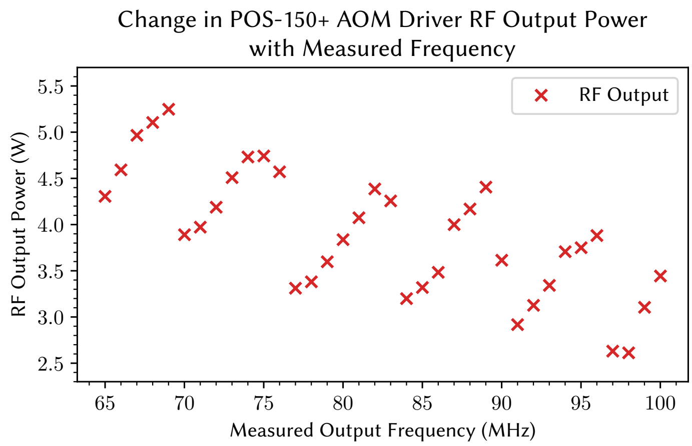

(b) Measured power of the output RF signal

Figure 4.6: Change in power of the output RF signal of the POS-150+ VCO-based AOM driver. Mode-like behaviour can be observed in the measured data.

4.2 Characterisation and Results

As previously discussed in subsection 3.2.1, a beam waist of 25 µm was targeted as a balance between the sweeping range and beam size. Using the selected lenses, and the calculations outlined in section 3.3 (input beam waist $w_0 = 0.5\,\text{mm}$), we expect to reach a beam waist w_0' of 20.44 µm. In the first iteration of the setup, a beam waist in the horizontal direction of $w_{0,\,\text{horz}} = (20.43 \pm 0.31)\,\mu\text{m} = (20.4 \pm 0.4)\,\mu\text{m}$ and a beam waist in the vertical direction of $w_{0,\,\text{vert}} = (22.61 \pm 0.13)\,\mu\text{m}$ were achieved, as can be seen in Figure 4.5. While $w_{0,\,\text{horz}}$ matches nicely with the expected beam waist, $w_{0,\,\text{vert}}$ differs significantly.

The discrepancies were not all that surprising, since the placement of the lenses, especially the final $f_3 = 200\,\text{mm}$ lens, were not very precise due to the large distances between each consecutive lens (575 mm and 700 mm respectively). The fact that $w_{0,\,\text{horz}} = (20.4 \pm 0.4)\,\mu\text{m}$ was so close to the theoretically expected value of $w_0' = 20.44\,\mu\text{m}$ was likely a happy coincidence.

4.2.1 Voltage-Controlled Oscillator-Based Implementation

The first implementation of the time-averaged ODT was done by using an in-house model POS-150+ VCO to drive the AOM. The VCO generates a sinusoidal RF signal with a frequency f_{AOM} based on a input voltage V_0. This input voltage was provided by a Rigol DG4162 function generator. A constant voltage was provided by generating a square wave with $f_{\text{mod}} = 1\,\mu\text{Hz}$ and a duty-cycle of 80.0 % and setting $V_{\text{high}} = V_0$. A multimeter was then used to monitor the output voltage directly. Such a setup was easy-to-implement and was sufficient for any static (not frequency modulated) measurements.

However, this configuration proved to be riddled with problems. Using an Anritsu MS2720T Spectrum Analyser (with two 10 dB Mini-Circuits attenuators = 20 dB attenuation), the power of the output RF signal from the AOM driver at different frequencies was measured. As we see in Figure 4.6, despite the amplifier setting being held constant, the power of the output RF signal varies greatly between 2.61 W and 5.25 W. An unexplained mode-like behaviour can also be observed in the data obtained. The power output of the AOM driver was thus too inconsistent to be used over a large sweeping range without sufficient compensation.

The frequency modulation was then turned on by modulating the voltage V_0 from the signal generator around 1.656 V (corresponding to 80 MHz) with a frequency of f_{mod} and a range of 3 V (i.e. $\pm 1.5\,\text{V} \equiv \pm 12.7\,\text{MHz}$). A ramp / sawtooth modulation was chosen. The frequency modulation was then varied from $f_{\text{mod}} = 1\,\text{kHz}$ to $f_{\text{mod}} = 400\,\text{kHz}$. The resulting spectrum was then measured with the Anritsu spectrum analyser. The measurement setup remained the same as depicted in Figure 4.6a.

The results obtained are depicted in Figures 4.7 and 4.8. In order to obtain the bandwidth of the top-hat-like spectrum at each modulation frequency f_{mod}, it was fitted to a rectangle function with error functions as the steps up and down, with A, μ_1, μ_2, σ_1 and σ_2 as the fit parameters:

$$f(x) = \frac{A}{2}\left[\operatorname{erf}\left(\frac{x-\mu_1}{\sigma_1}\right) + \operatorname{erf}\left(-\frac{x-\mu_2}{\sigma_2}\right)\right] \tag{4.1}$$

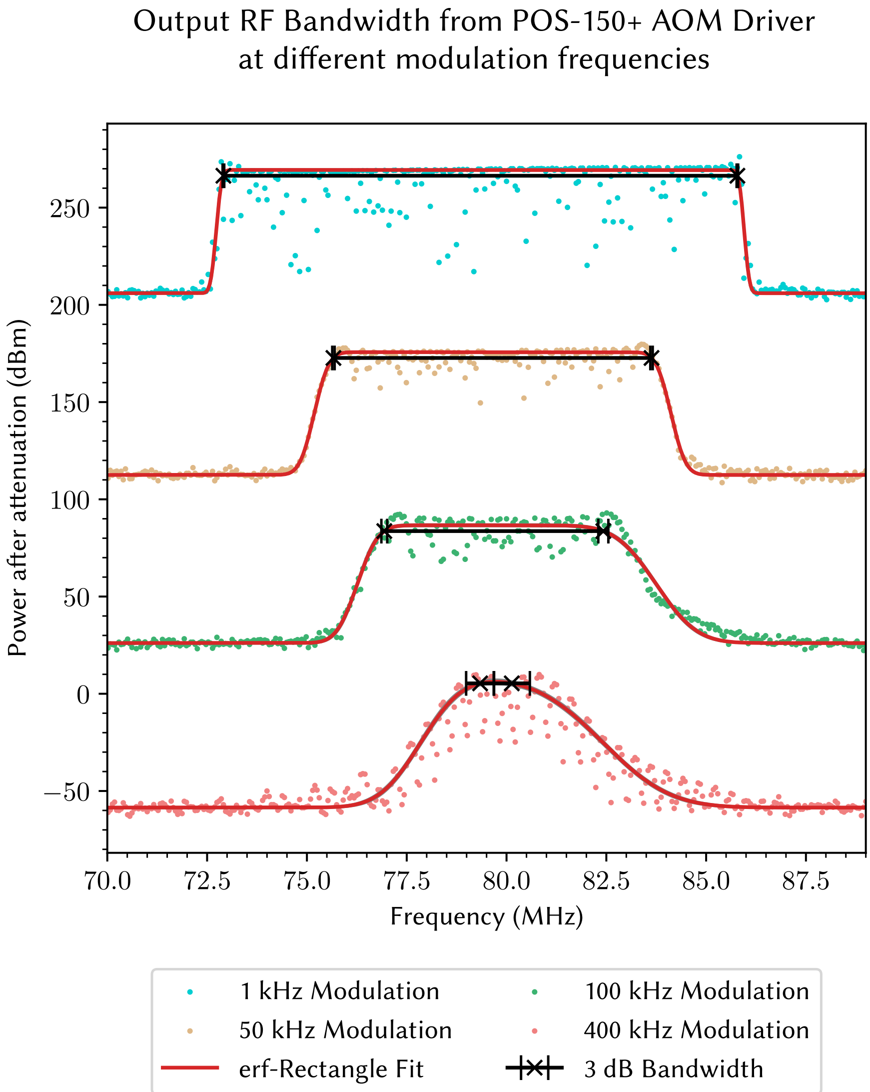

Figure 4.7: Bandwidth of RF Response of the VCO in the POS150+ AOM driver. In the plot, the power values are offset by 90 dBm between each set of measurement. From top to bottom, the baselines are 270 dBm, 180 dBm, 90 dBm, and 0 dBm respectively.

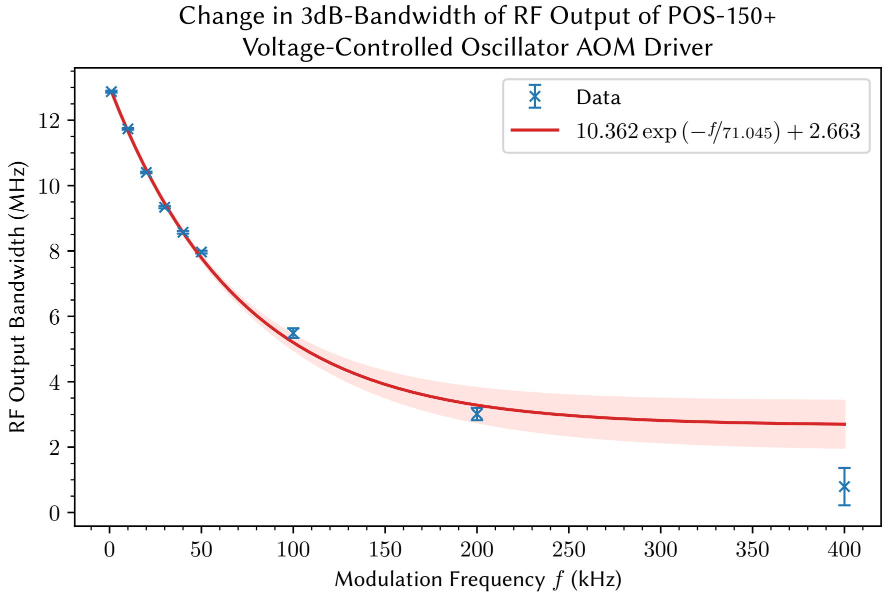

Figure 4.8: Change in Bandwidth of RF Response of the VCO in the POS150+ AOM driver. Shaded area represents confidence interval.

The 3 dB bandwidth was then calculated from the fit. From Figure 4.8, we see that the spectral bandwidth of the output RF signal decreases exponentially with the modulation frequency, with the bandwidth decreasing by half approximately every (49 ± 5) kHz.

The modulation depth of the VCO output thus appears to decrease significantly as the modulation frequency increases. In other words, the oscillator was unable to follow the tuning voltage instantaneously. This restriction of the modulation bandwidth of the VCO made it unsuitable for use with the ODT.

4.2.2 High Frequency Modulation and Vector Signal Generator-Based Implementation

The improved iteration of the setup involved the use of an Agilent N5182A MXG Vector Signal Generator to generate the RF signal instead of a VCO. The generated RF signal was then amplified with an RF amplifier before going to the AOM. This setup is outlined in Figure 4.9.

To modulate the frequency f_{AOM} of the RF signal and thus the position x' of the resulting beam, another signal generator was used to generate an oscillating signal with frequency f_{mod} around 0 V. The vector signal generator then modulates the frequency f_{AOM} of the output with the oscillating input voltage (*FM Signal*) from the second signal generator.

To modulate how much the signal was amplified, the second signal generator also provided another (potentially oscillating) signal (*AM Signal*) that goes to the amplfier.

Although not strictly necessary, it was advantageous that the FM and AM signals were generated from the same signal generator. This way, the two signals may be phase-matched for

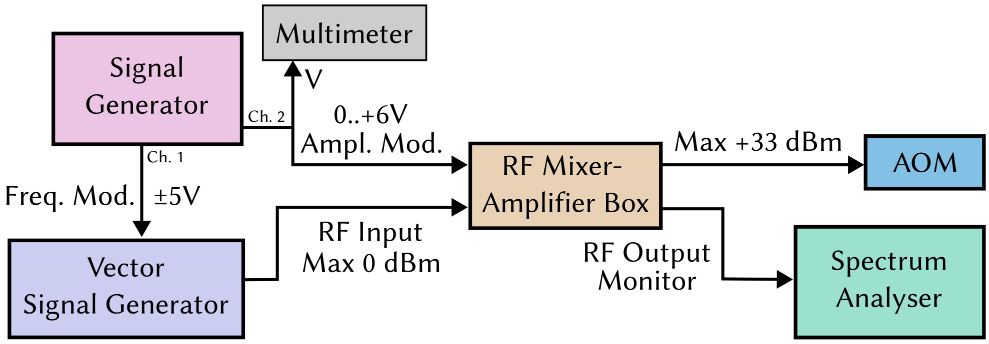

Figure 4.9: Improved AOM driver setup with a vector signal generator used for high frequency modulations

certain applications, such as to compensate for a non-homogenous response of the amplifier as a function of the AOM driving frequency f_{AOM}.

With this setup, much higher modulation frequencies f_{mod} could be realised. Instead of the reduction in output RF signal bandwidth like with the VCO, we observed the formation of sidebands that were f_{mod} apart, albeit only at a small enough resolution bandwidth (RBW). At larger RBW settings, these sidebands were subject to aliasing and were unrecognisable. A representative spectrum measurement is depicted in Figure 4.10.

At modulation frequencies f_{mod} higher than $\approx 1\,\text{MHz}$, instead of a smooth, elongated beam profile, the position of the sidebands in the spectrum seem to determine exactly where the beam would be observed. The exposure time on the CCD was set to 0.5 ms, hence it was unlikely for

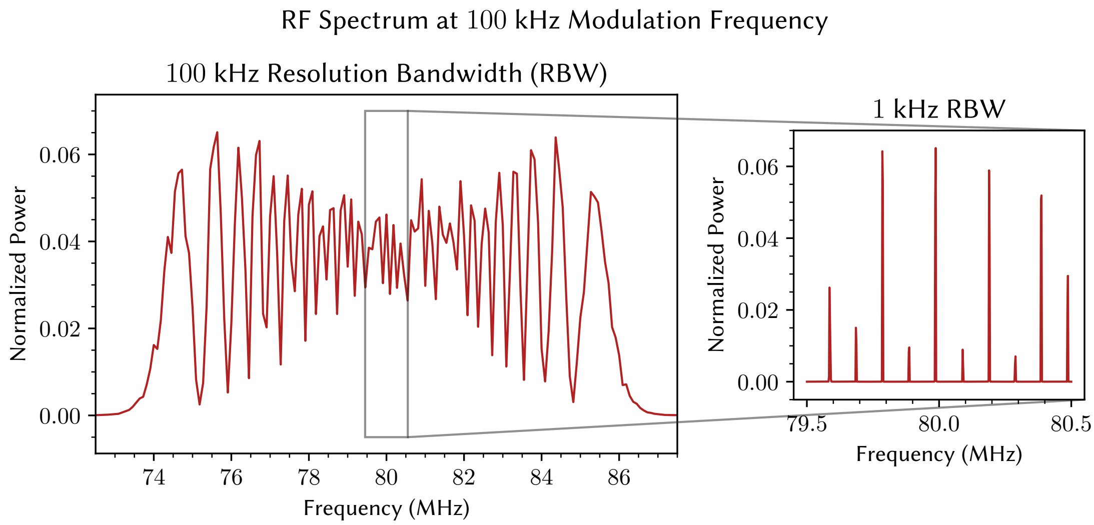

Figure 4.10: Spectrum of RF output at $f_{\text{mod}} = 100\,\text{kHz}$ modulation. Power was normalised to the maximum power measured by the spectrum analyser in the Figure 4.11. If we increase the resolution bandwidth (RBW) to 1 kHz and zoom in, we see that the peaks are almost exactly f_{mod} apart.

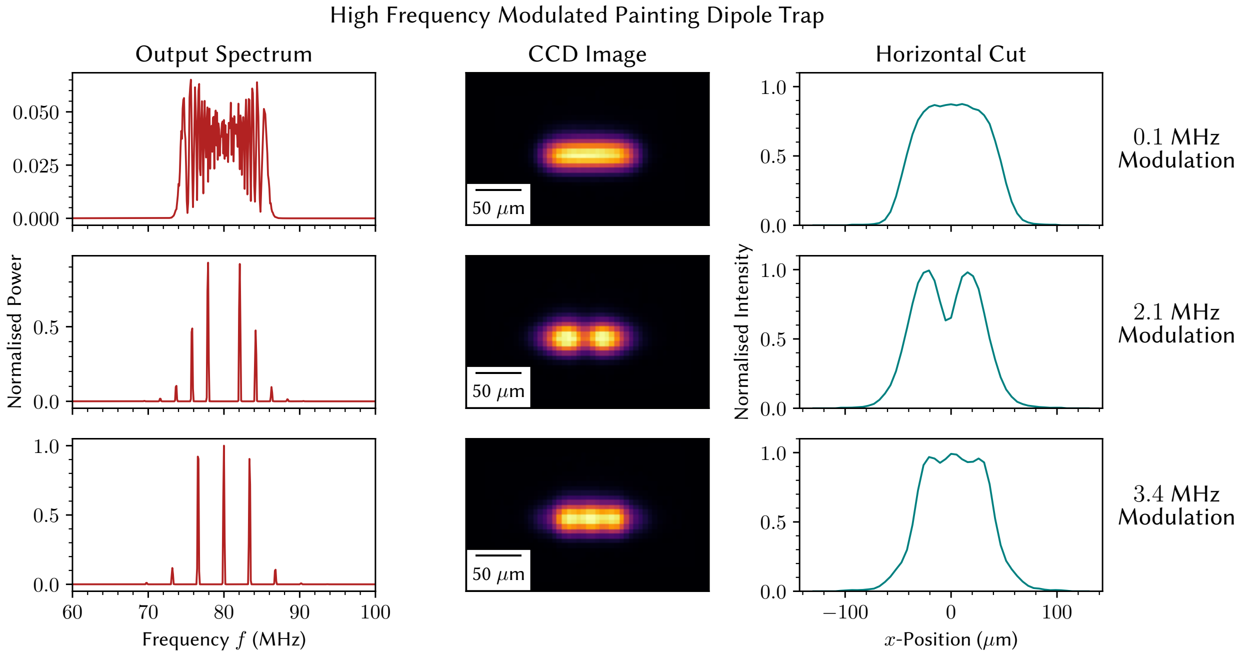

Figure 4.11: Beam profile and RF spectrum at high modulation frequencies. Power was normalised to the maximum power measured by the spectrum analyser in these three datasets. Instead of a continous beam profile, we notice that the beam seem to only appear at certain positions corresponding to the spectrum measured. At $f_{\text{mod}} = 2.1\,\text{MHz}$, the central beam completely disappears. An optimal modulation frequency of $f_{\text{mod}} = 3.4\,\text{MHz}$ was found.

aliasing at the CCD to be the cause of this observation.

A representative measurement of the abovementioned phenomenon was performed with the settings outlined in Table 4.2, and illustrated in Figure 4.11. An optimal f_{mod} of $3.4\,\text{MHz}$ was found. At this f_{mod}, the three beam positions overlap with one another in a way that approximates an elongated beam profile, providing the extended ODT that this thesis hoped to achieve.

One possible explanation of the appearance of these distinct points instead of a smooth time-averaged profile is the non-vanishing interaction time between the acoustic wave in the AOM crystal and the incoming light. Since the modulation frequency f_{mod} was so high, in the time needed for the acoustic wave to travel across the diameter of the incoming light beam, the photons in the light beam would have interacted with phonons of many different frequencies instead of just a single, instantaneous frequency, thus resulting in an effective spectrum as measured by the spectrum analyser.

Another possible explanation is hinted at by Albers in his dissertation [37]. In equation (3.18), he defines the upper limit of the modulation frequency to be

$$f_{\text{mod}} \ll \frac{w_0}{\delta x} \tag{4.2}$$

Device	Parameter	Set Value
FM[7] Signal Generator	Waveform	Ramp
	Frequency	f_{mod}
	Symmetry	50.0 %
	Amplitude[8]	2.5 V
	Offset	0 V
AM[9] Signal Generator	Waveform	Square
	Frequency	1 µHz
	Duty Cycle	80.0 %
	Voltage V_{high}	3.5 V
	Voltage V_{low}	0 V
Vector Signal Generator	Central Frequency	80 MHz
	Deviation Depth	10 MHz
	Output Power	0 dBm

Table 4.2: Settings of the signal generators for Figure 4.11 high frequency modulations.

In the above equation, w_0 is the waist of the unmodulated beam in the final imaging plane, and δx is the change in the final position of the beam per change in AOM driving frequency f_{AOM}, given in µm MHz^{-1}. He explains that when the driving frequency f_{AOM} is modulated, the spectrum driving the AOM will have sidebands around the central frequency separated by the modulation frequency f_{mod}. The diffraction of light as a result of these sidebands then causes a position shift of $(\delta x \cdot f_{\text{mod}})$. Thus, to ensure this position shift is not more than the beam waist at the final focal plane, he imposes this upper limit on f_{mod}.

For the AOM and lens system used in this thesis, the change in position per change in AOM driving frequency may be calculated from equation (3.6) to obtain $\delta x = 7.58\,\mu\text{m}\,\text{MHz}^{-1}$. Therefore, should this other explanation be correct, then the limit for a final unmodulated beam waist of 25 µm is given by $f_{\text{mod}} \ll 3.29\,\text{MHz}$, regardless of the size of the beam going through the AOM.

As the concrete explanation behind this observation is still unclear, more investigation still needs to be conducted.

[7] Frequency modulation
[8] On the oscilloscope "Amplitude" means 2×Amplitude (i.e. Amplitude $= 2.5\,\text{V} = \pm 1.25\,\text{V}$)
[9] Amplitude modulation

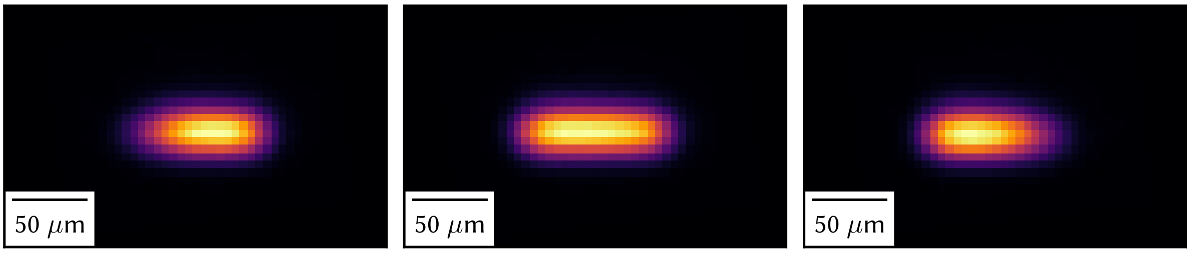

(a) 100 kHz, ramp AM, $\Delta\varphi = 0°$ (b) 100 kHz, no AM (const. 3 V) (c) 100 kHz, ramp AM, $\Delta\varphi = 180°$

Figure 4.12: Amplitude modulation from 0 V to 3 V phase-matched with the modulation frequency such that $f_{\text{mod}} = f_{\text{AM}}$ and $\varphi_{\text{mod}} = \varphi_{\text{AM}} + \Delta\varphi$. Except for the amplitude modulation (AM) settings, all settings were the same as in Table 4.2. This can help to create specific trap shapes, or compensate for any inhomogeneity in the amplifier/AOM response as a function of the AOM driving frequency f_{AOM}.

4.3 Proposed Setup for the FermiQP Machine

For the final FermiQP machine, a setup similar to the PoC setup presented above is proposed, including the use of a single signal generator for the frequency and amplitude modulation.

By carefully designing the waveforms of the frequency and the amplitude modulations, traps of arbitary form may be realized. Furthermore, a direct current (DC) offset may be put on the amplitude modulation to power-stabilize the light going to the ODT. A demonstration of the amplitude modulation is depicted in Figure 4.12.

Due to the relatively large spectral linewidth of the IPG laser, it would also be advantageous to replace the plano-convex lenses with achromatic doublets to reduce any chromatic aberration.

Furthermore, the optical power of the infrared light used in the PoC setup was five orders of magnitude less than the proposed laser power that the final setup should have. Due to intensity-related changes to the optical path, such as thermal lensing within the AOM crystal, we expect some minor changes to the PoC setup in terms of distances and optical components for the final setup.

The final proposed setup is outlined in Figure 4.13.

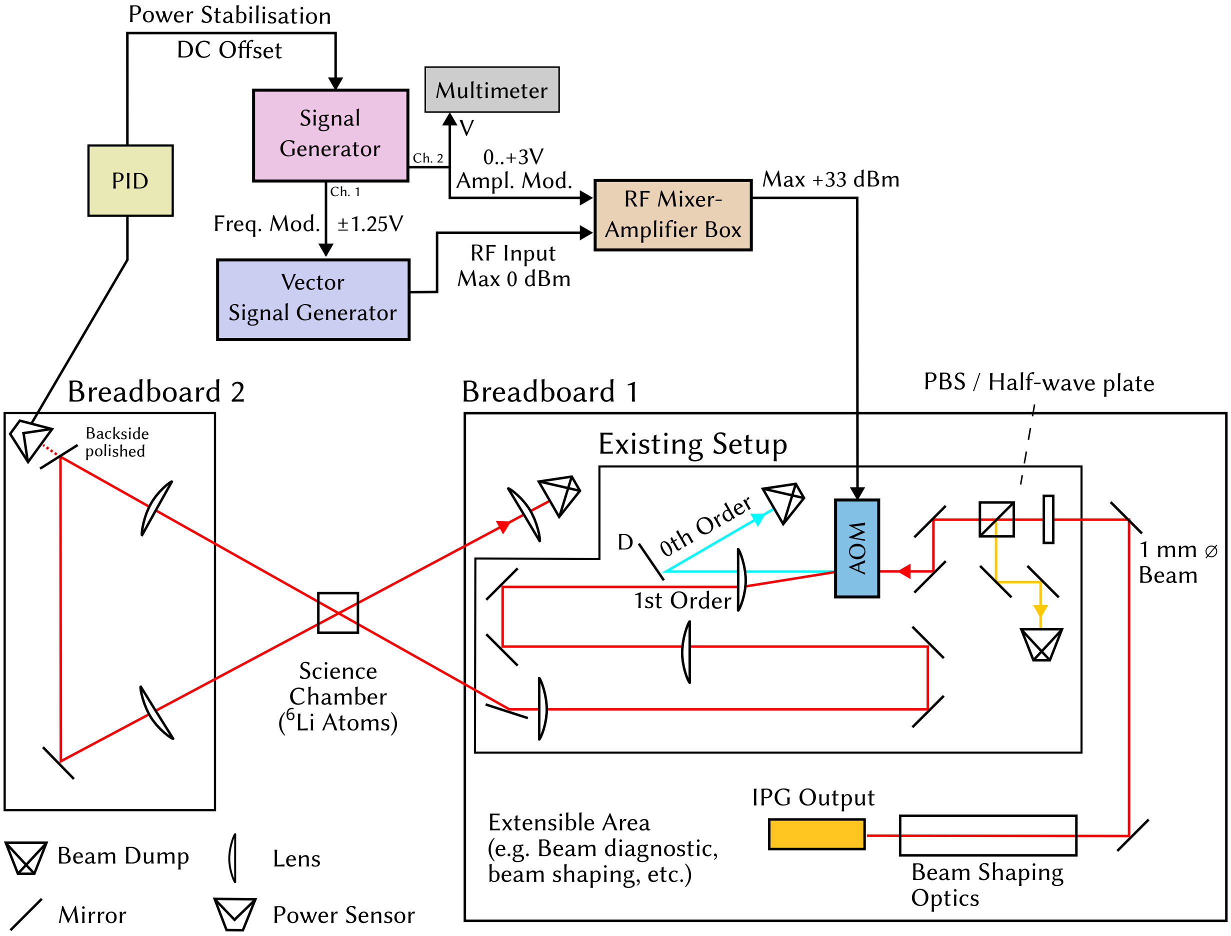

Figure 4.13: Final setup proposal for the FermiQP machine.

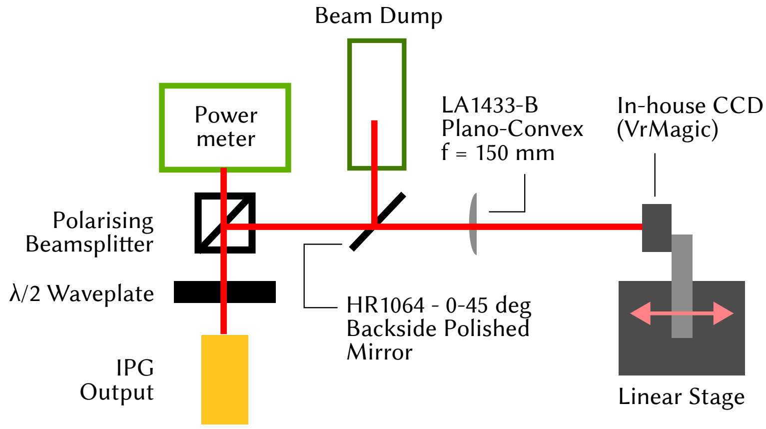

Figure 4.14: Optomechanical setup used for the measurement of the M^2 of the IPG laser. The power on the IPG laser was set to 20 % and attenuated first with a $\lambda/2$-waveplate–PBS combination and then a backside polished mirror. The reading on the powermeter was $\approx 25\,\mathrm{W}$, with $\approx 13.5\,\mathrm{mW}$ going into the CCD camera.

4.4 Characterisation of the High-Power IPG Laser

In this section, some characterisation of the high-power IPG laser is presented. These information will be relevant for the final implementation of the ODT in the FermiQP machine.

The IPG laser is a diode-pumped spatially single-mode, spectrally multi-mode linearly polarized CW Ytterbium fibre laser. It is water-cooled and has a designed maximum output power of 200 W. The actual maximum power of the laser was measured to be 198 W[10]. This deviates from the measurement of 206 W provided by the manufacturer [45], but does not impact the functionality of the laser with respect to implementation of the ODT.

The M^2 beam quality factor of the IPG laser was characterised using the setup depicted in Figure 4.14. The power of the IPG laser was set to 20 %, which corresponds to an output power of 27.7 W. This output was then attenuated using a $\lambda/2$-waveplate–PBS combination and a HR1064 - 0-45 deg backside polished mirror.

The reading on the powermeter was $\approx 25\,\mathrm{W}$, resulting in $\approx 2.7\,\mathrm{W}$ of power going to the backside polished mirror. With a reflectivity R of at least $99.5\,\%$ specified by the manufacturer [51], we get a laser power P of $< 13.5\,\mathrm{mW}$ going through a Thorlabs LA1433-B plano-convex lens ($f = 150\,\mathrm{mm}$) into the CCD camera. An in-house beamprofiler program was then used to do a 2D Gaussian fit on the image to obtain the beam diameter in each axis at several position along the propagation direction.

The data was then fitted to the Gaussian beam propagation equation (Equation 2.12). The fit result is depicted in Figure 4.15. From the fit, we obtain the results in Table 4.3.

The beam waists obtained differ significantly from the expected beam waist w_0 of 22.5 µm based on the optical setup, but that could easily be attributed to the less-than-ideal M^2 value. The measured M^2 results were also within the specifications of the manufacturer ($M^2 < 1.1$). [45]. This M^2 measurement helps us to better understand the laser and better predict its behaviour in the final setup.

Axis	M^2	Beam Waist (µm)
Horizontal	1.033 ± 0.017	23.8 ± 0.4
Vertical	1.066 ± 0.014	24.3 ± 0.4

Table 4.3: Fit results of the IPG laser M^2 Measurement. Uncertainties are from the fit.

[10] See Appendix C for more information on the power of the IPG laser

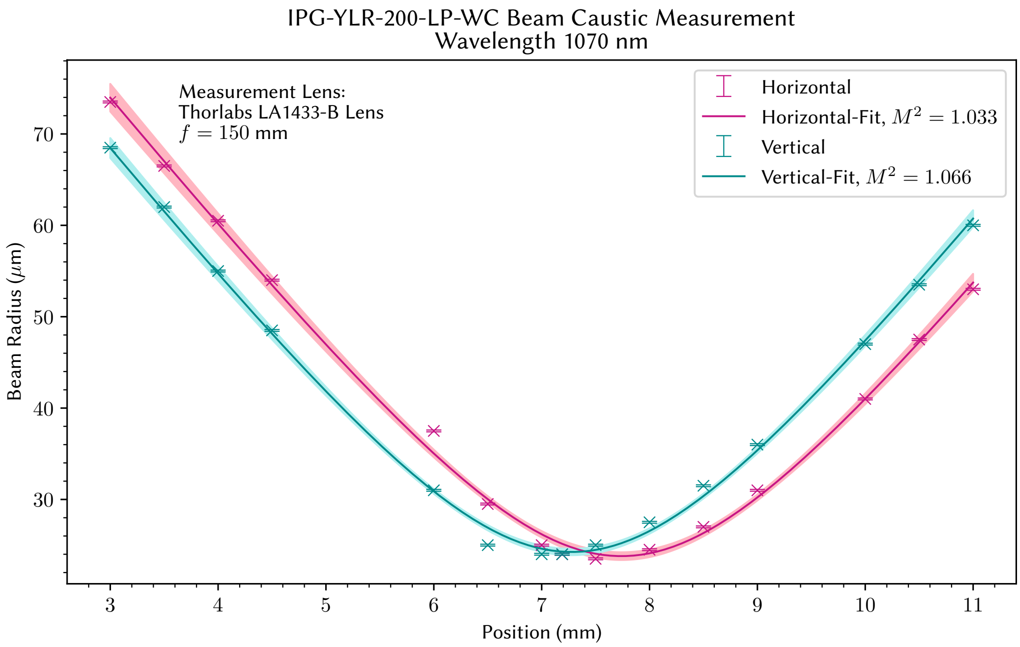

Figure 4.15: M^2 measurement and fit result. An error of $\pm 0.1\,\mu\text{m}$ was estimated for the beam radius. Shaded area represents confidence interval.

Chapter 5

Conclusion and Outlook

5.1 Summary

When it comes to trapping and cooling neutral atoms with an optical dipole trap (ODT), one of the many challenges is the balancing of trapping volume and cooling efficiency. Dynamic time-averaged optical potentials have proven to be especially useful in this respect by accelerating the process of evaporative cooling [37].

In this work, a time-averaged crossed-beam ODT with high frequency modulation was presented as the proposed design for the ODT in the FermiQP machine, which aims to realise a fermionic quantum processor simultaneously capable of analogue and digital operations using ultracold ^{6}Li atoms.

The feasibility of the abovementioned ODT was demonstrated through the construction of a proof-of-concept setup using a 1064 nm diode-pumped solid-state (DPSS) laser. By rapidly modulating the driving frequency f_{AOM} of an acousto-optic modulator (AOM) at $f_{\mathrm{mod}} = 3.4\,\mathrm{MHz}$ around the central frequency $f_{\mathrm{AOM.\,cent}} = 80\,\mathrm{MHz}$, a single-beam time-averaged potential with a vertical cross-sectional area approximately *three times* that of the static beam was attained.

With such a high modulation frequency, the only main factor limiting the thermal energy of the atoms captured is the trap depth. Furthermore, this kind of setup allows the ODT to have a large initial trapping volume, while simultaneously having the ability to dynamically reduce its size and compress the atoms during evaporative cooling. The increased density of the cold atoms speeds up thermalisation, thereby reducing the time needed to evaporatively cool the atoms to the degenerate quantum gas necessary for the next stage of the experiment. As such, it is capable of much more efficient loading, and subsequent cooling, of cold ^{6}Li atoms from a 3D magneto-optical trap (MOT) compared to a static crossed-beam dipole trap, thereby promising shorter cycle times of experiments.

5.2 Outlook

The ultimate goal of this thesis was to design a time-averaged ODT for use in the FermiQP experiment. In this experiment, ^{6}Li atoms will be trapped and cooled via a series of different techniques, before being loaded into an optical lattice for use in quantum simulation and quantum computation. During this process, the ^{6}Li atoms will be loaded from a 3D MOT into the time-averaged ODT, which will be used to quickly and effectively cool ^{6}Li atoms to a degenerate quantum gas using evaporative cooling, thus constituting an integral part of the larger experiment to realise a combined analogue and digital quantum processor.

While the proof-of-concept setup was very successful in demonstrating the feasibility of the proposed ODT with high frequency modulation, many parameters used within the setup still need to be optimised for the final ODT with the IPG laser, where a much higher optical power is to be used.

Once higher powers within the setup are realised, the ODT may then also be tested within a vacuum chamber with actual ^{6}Li atoms to evaluate its efficacy.

Furthermore, at very high modulation frequencies above $1\,\mathrm{MHz}$, a discrete time-averaged potential was observed, instead of a smooth continuous intensity distribution that was expected. In the previous chapter, two possible explanation of the observation were proposed.

Should this simply be a result of the finite interaction time between the photons of the laser beam and the phonons in the AOM cystal, a change in the design of the optical system to further reduce the diameter of the beam going through the AOM could theoretically decrease the interaction time and increase the limit after which the continuous beam profile becomes discrete.

On the other hand, the alternative explanation alluded to by Albers in his dissertation [37] suggests that the modulation sidebands observed on the spectrum analyser will always appear in the imaging plane as distinct beams, separated by a fixed distance which is proportional to the modulation frequency f_{mod}. As such, one needs to ensure that the distance between these distinct beams is not larger than one beam waist. Should this explanation be correct, then changing the size of the beam going through the AOM would not affect the results.

Therefore, to have a better understanding of this phenomenon, including the conditions and limits of each regime, further investigation is needed. Perhaps, it is even possible to obtain a smooth, continuous beam profile with a megahertz modulation frequency.

The codes used in this thesis are made available for archival purposes at [52].

Appendix A

Diffraction Efficiency of the Acousto-optic Modulator (AOM) Used

An acousto-optic modulator (AOM) typically has different diffraction efficiencies at different frequencies f_{AOM} of input radio frequency (RF) signal. To characterise this behaviour and understand how large the tuning range for our AOM is, the optical power in the first order was measured at different RF input power and frequencies using the setup described in Figure 4.9. This would allow us to find the bandwidth and subsequently understand how much we can deflect the beam to create the spatial modulation required for the sweeping optical dipole trap (ODT). The results of the aforementioned measurement are depicted in Figure A.1.

For the measurement, the amplitude modulation (AM) voltage was set to 3.25 V and the optical power was averaged across 3000 datapoints that span approximately 5 min to ensure that fluctuations in the intensity of the diode-pumped solid-state (DPSS) laser does not influence our results.

From the plot, we see that the diffraction efficiency curve is not symmetrical around the central frequency of $f_{\mathrm{AOM,\,cent}} = 80\,\mathrm{MHz}$. Instead, the curve has a long tail towards the higher frequencies but falls off comparatively sharply towards to the lower frequencies. Thus, a larger tuning range with reasonable diffraction efficiencies could only be achieved if it is not symmetrical about the peak frequency of $f_{\mathrm{AOM,\,cent}} = 80\,\mathrm{MHz}$. The vendor-specified operation frequency of (80 ± 5) MHz however does generally agree with the measurements that have been taken here.

Since the Agilent vector signal generator allows the generation of arbitrary waveforms, one may also choose to drive the AOM with a frequency/power combination that follows along one of the contour lines of the plot in Figure A.1 in order realise a larger spatial modulation of the beam while having constant optical power at the atoms.

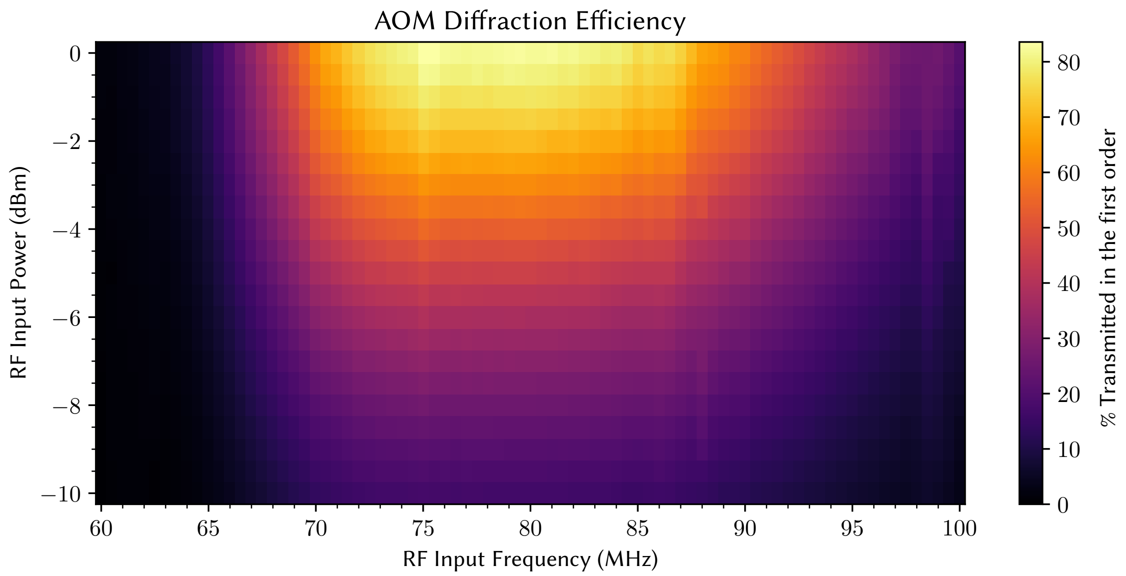

Figure A.1: Diffraction efficiency of the 3080-194 acousto-optic modulator (AOM) from Crystal Technology, Inc.. The power of the Agilent vector signal generator was changed to obtain the AOM diffraction efficiency at different RF input power.

Appendix B

Response Map of the Radio Frequency (RF) Mixer-Amplifier Box AOM Driver

In order to obtain reasonable settings for the radio frequency (RF) mixer-amplifier box used to drive the acousto-optic modulator (AOM) for the optical dipole trap (ODT), a response map was measured.

To obtain the measurement, the value of each parameter was varied as follows:

- The amplitude modulation (AM) voltage:
  $V = 0.50\,\mathrm{V}$ to $V = 6.00\,\mathrm{V}$ in steps of 0.25 V.
- The RF input power on the Agilent vector signal generator:
  $P = -20.0\,\mathrm{dBm}$ to $P = 0.0\,\mathrm{dBm}$ in steps of 0.5 dBm.
- The RF input frequency on the Agilent vector signal generator:
  $f_{\mathrm{AOM}} = 55.0\,\mathrm{MHz}$ to $f_{\mathrm{AOM}} = 105.0\,\mathrm{MHz}$ in steps of 0.5 MHz.

The results can be seen in Figure B.1. For each plot, the resultant RF output powers measured were grouped by two variables, and the average was taken over the third (and last) variable.

From the results, it seems that the use of an RF input power of $P \approx -1\,\mathrm{dBm}$ and modulating the AM voltage between 0 V and 3 V results in the most tuning range.

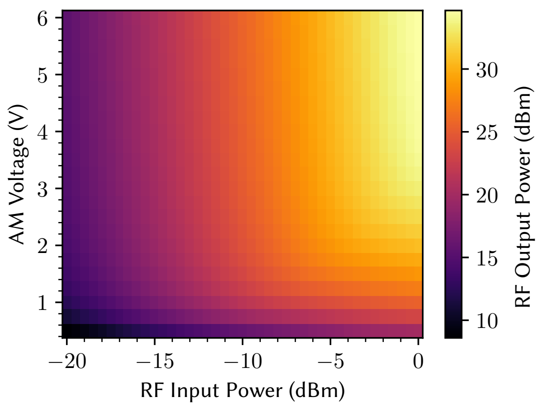

(a) AM voltage against input RF power averaged over all RF frequencies. For $V > 3\,\mathrm{V}$, changing the AM voltage has little effect on the output, making this range unsuitable for AM.

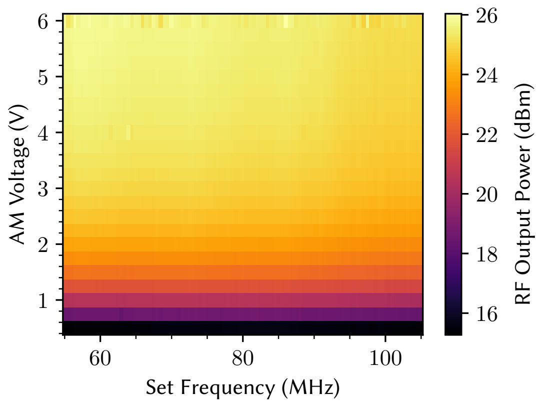

(b) AM voltage against input RF frequency averaged over all RF input powers. The response is rather homogeneous in the frequency here, except around $V \approx 6\,\mathrm{V}$. As the output RF power saturated at relatively low AM voltages, the tuning range for AM seem to be the best for $V < 3\,\mathrm{V}$.

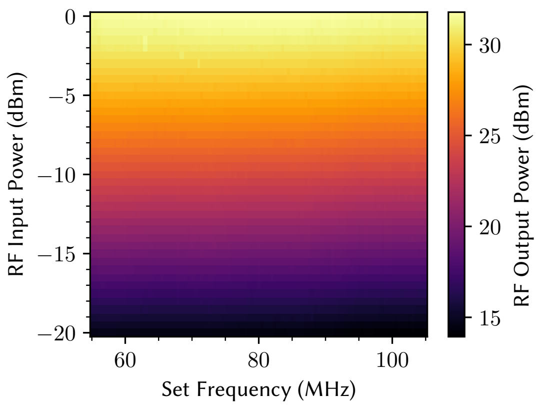

(c) Input RF power against input RF frequency averaged over all AM voltages. A slight inhomogeneous response in the frequency can be observed here.

Figure B.1: Response of the RF mixer-amplifier box used to drive the AOM. This provides helpful insights into reasonable values to use for experiments.

Appendix C

Power Measurements of the YLR-200-LP-WC IPG Laser

The measurement of the power of the IPG laser at different set points on the laser controller was done by Qesja [53] by measuring the laser output power after a $\lambda/2$-waveplate. The $\lambda/2$-waveplate was turned until the measured power was maximized. The results obtained were then compared to the data from a test report from the manufacturer (labelled "Report"). The results are listed in Table C.1 and plotted in Figure C.1. This data is relevant for the final implementation of the proposed optical dipole trap (ODT) in the experiment using the IPG laser.

The lowest set point on the IPG laser controller was 12 %.

Set Point (%)	Monitored Power (W)	Measured Power (W)	Measured Power (Report) (W)	Monitored Power (Report) (W)
12.0	9.37	9.32	11.4	9.5
20.0	27.6	27.7	29.6	28.1
30.0	50.4	50.3	52.7	51.5
40.0	73.3	73.2	76.1	74.8
50.0	96.0	95.9	97.1	97.6
60.0	118.0	117.6	119.5	121.0
70.0	141.0	139.3	141.6	144.0
80.0	164.0	160.1	163.4	165.0
90.0	185.0	180.0	184.8	187.0
95.0	196.0	189.0	—	—
100.0	207.0	198.0	206.0	209.0

Table C.1: IPG Power Measurements

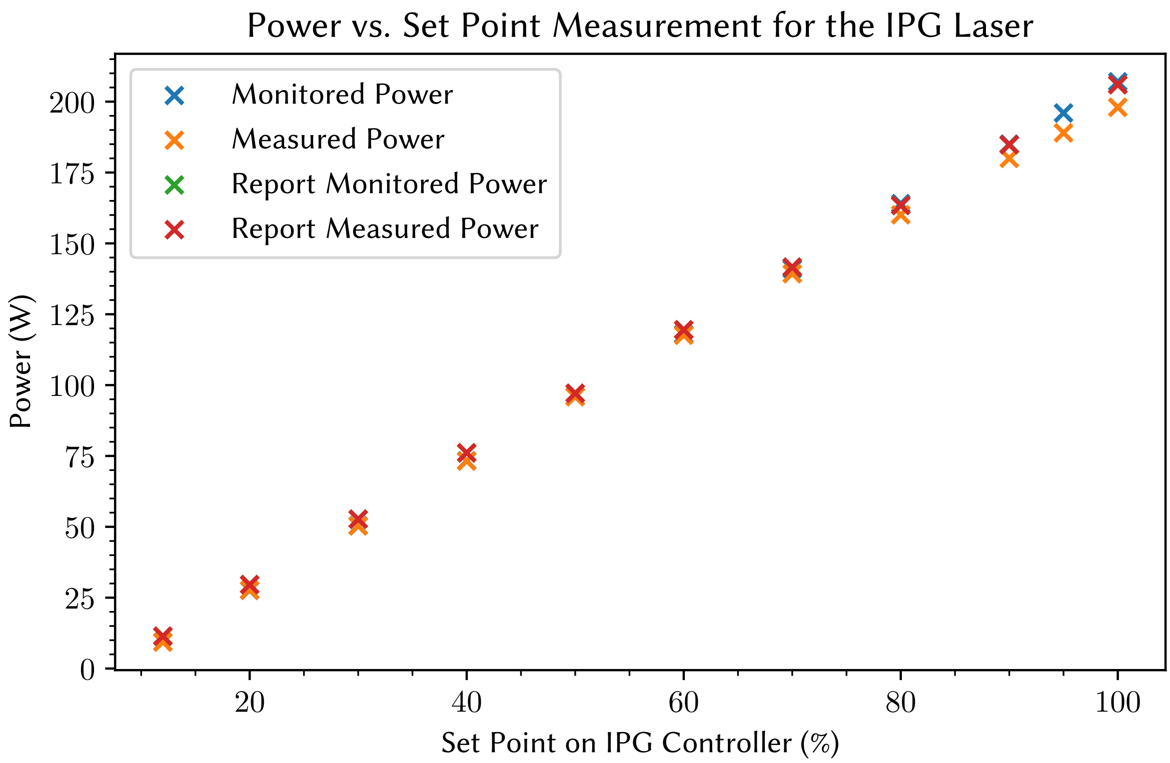

Figure C.1: IPG power measurements

Appendix D

Lens Specifications within the Experimental Realisation

In the proof-of-concept (PoC) setup, the following lenses from Thorlabs were used: LA1608-B ($f_1 = 75\,\mathrm{mm}$), LA1908-B ($f_2 = 500\,\mathrm{mm}$), LA1708-B ($f_3 = 200\,\mathrm{mm}$). These are lenses with a "B" anti-reflective (AR) coating, which were only rated for wavelengths between 650 nm and 1050 nm.

Despite the "incorrect" AR coatings, these lenses were reasonable substitutes for more suitable ones that were unavailable at the time. This is because the important optical properties of these lenses (reflectance and refractive index) do not differ significantly at 1064 nm compared to the specified working range. This is depicted in Figure D.1.

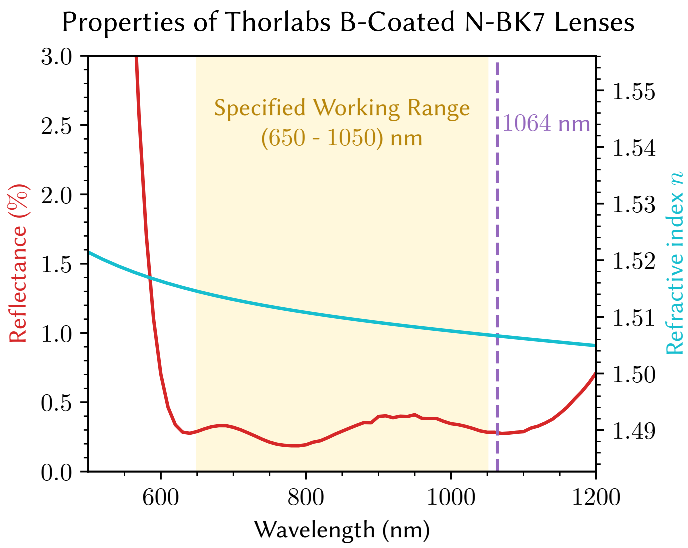

Figure D.1: Properties of Thorlabs "B" anti-reflective (AR) coated N-BK7 lenses [54, 55]

Acronyms

AM amplitude modulation. 39, 45, 47, 48
AOM acousto-optic modulator. vii, 15–19, 23, 27, 29, 32–39, 43–48
AR anti-reflective. 51
CCD charge-coupled device. 29, 30, 36, 37, 40, 41

CW continuous wave. 20, 27, 41
DPSS diode-pumped solid-state. 4, 27–29, 43, 45

FermiQP Fermion Quantum Processor. vii, 2, 17, 18, 27, 39–41, 43, 44

IR infrared. 29

MOT magneto-optical trap. 2, 17, 20, 43, 44

ND neutral-density. 30

ODT optical dipole trap. vii, 2–6, 8, 10, 11, 13, 14, 17, 18, 20, 21, 24, 25, 27, 31, 33, 35, 37, 39, 41, 43–45, 47, 49

PBS polarising beamsplitter. 27, 40, 41

PM polarisation maintaining. 27
PoC proof-of-concept. 4, 27, 28, 31, 39, 51
RBW resolution bandwidth. 36, *Glossary:* Resolution Bandwidth

RF radio frequency. 15, 16, 29, 32–37, 45–48
VCO voltage-controlled oscillator. 29, 32–36

Glossary

M^2 M-Squared Beam Quality Factor, see Equation 2.12. 22–25, 40–42

dBm or Decibel-milliwatts Unit of power level expressed in decibels (dB) with reference to 1 mW. This means that $0\,\mathrm{dBm} = 1\,\mathrm{mW}$ and $P(x \text{ in dBm}) = 1\,\mathrm{mW} \cdot 10^{x/10}$. 34

IPG laser 200 W YLR-200-LP-WC diode-pumped spatially single-mode, spectrally multi-mode linearly polarized continuous wave Ytterbium fibre laser manufactured by IPG Photonics. 20, 21, 27, 29, 39–41, 44, 49

Resolution Bandwidth Resolution Bandwidth (RBW) is the bandwidth of the filter of a heterodyne receiver. It defines the frequency resolution of the resulting spectrum. [56]. 36

Bibliography

[1] Richard P. Feynman. “Simulating Physics with Computers”. In: *International Journal of Theoretical Physics* 21.6 (June 1982), pp. 467–488. ISSN: 1572-9575. DOI: 10.1007/BF02650179.

[2] I. M. Georgescu, S. Ashhab and Franco Nori. “Quantum Simulation”. In: *Reviews of Modern Physics* 86.1 (Mar. 2014), pp. 153–185. DOI: 10.1103/RevModPhys.86.153.

[3] Yuri Manin. *Computable and Uncomputable (Вычислимое и невычислимое)*. Moscow, USSR: Soviet Radio, 1980.

[4] B. Apolloni, C. Carvalho and D. de Falco. “Quantum Stochastic Optimization”. In: *Stochastic Processes and their Applications* 33.2 (Dec. 1989), pp. 233–244. ISSN: 0304-4149. DOI: 10.1016/0304-4149(89)90040-9.

[5] Tadashi Kadowaki and Hidetoshi Nishimori. “Quantum Annealing in the Transverse Ising Model”. In: *Physical Review E* 58.5 (Nov. 1998), pp. 5355–5363. DOI: 10.1103/PhysRevE.58.5355.

[6] Adriano Barenco et al. “Elementary Gates for Quantum Computation”. In: *Physical Review A* 52.5 (Nov. 1995), pp. 3457–3467. DOI: 10.1103/PhysRevA.52.3457.

[7] Andrew A. Houck, Hakan E. Türeci and Jens Koch. “On-Chip Quantum Simulation with Superconducting Circuits”. In: *Nature Physics* 8.4 (Apr. 2012), pp. 292–299. ISSN: 1745-2481. DOI: 10.1038/nphys2251.

[8] Immanuel Bloch, Jean Dalibard and Sylvain Nascimbène. “Quantum Simulations with Ultracold Quantum Gases”. In: *Nature Physics* 8.4 (Apr. 2012), pp. 267–276. ISSN: 1745-2481. DOI: 10.1038/nphys2259.

[9] R. Blatt and C. F. Roos. “Quantum Simulations with Trapped Ions”. In: *Nature Physics* 8.4 (Apr. 2012), pp. 277–284. ISSN: 1745-2481. DOI: 10.1038/nphys2252.

[10] D. Jaksch et al. “Cold Bosonic Atoms in Optical Lattices”. In: *Physical Review Letters* 81.15 (Oct. 1998), pp. 3108–3111. DOI: 10.1103/PhysRevLett.81.3108.

[11] D. Jaksch et al. “Entanglement of Atoms via Cold Controlled Collisions”. In: *Physical Review Letters* 82.9 (Mar. 1999), pp. 1975–1978. DOI: 10.1103/PhysRevLett.82.1975.

[12] H.-J. Briegel et al. “Quantum Computing with Neutral Atoms”. In: *Journal of Modern Optics* 47.2-3 (Feb. 2000), pp. 415–451. ISSN: 0950-0340, 1362-3044. DOI: 10.1080/09500340008244052. arXiv: quant-ph/9904010.

[13] Ivan H. Deutsch, Gavin K. Brennen and Poul S. Jessen. “Quantum Computing with Neutral Atoms in an Optical Lattice”. In: *Fortschritte der Physik* 48.9-11 (Sept. 2000), pp. 925–

943. ISSN: 00158208, 15213978. DOI: 10.1002/1521-3978(200009)48:9/11<925::AID-PROP925>3.0.CO;2-A. arXiv: quant-ph/0003022.

[14] Manuel Gerken. "Gray Molasses Cooling of Lithium-6 Towards a Degenerate Fermi Gas". MA thesis. Heidelberg, Germany: University of Heidelberg, 2016.

[15] A. Burchianti et al. "Efficient All-Optical Production of Large ^{6}Li Quantum Gases Using D_1 Gray-Molasses Cooling". In: *Physical Review A* 90.4 (Oct. 2014), p. 043408. DOI: 10.1103/PhysRevA.90.043408.

[16] G. A. Askar'yan. "Effect of the Gradient of a Strong Electromagnetic Ray on Electrons and Atoms (Воздействие градиента поля интенсивного электромагнитного луча на электроны и атомы)". In: *Zhur. Eksptl'. i Teoret. Fiz.* 42.6 (June 1962), pp. 1567–1570.

[17] A. Ashkin. "Acceleration and Trapping of Particles by Radiation Pressure". In: *Physical Review Letters* 24.4 (Jan. 1970), pp. 156–159. DOI: 10.1103/PhysRevLett.24.156.

[18] A. Ashkin. "Trapping of Atoms by Resonance Radiation Pressure". In: *Physical Review Letters* 40.12 (Mar. 1978), pp. 729–732. DOI: 10.1103/PhysRevLett.40.729.

[19] J. E. Bjorkholm et al. "Observation of Focusing of Neutral Atoms by the Dipole Forces of Resonance-Radiation Pressure". In: *Physical Review Letters* 41.20 (Nov. 1978), pp. 1361–1364. DOI: 10.1103/PhysRevLett.41.1361.

[20] Steven Chu et al. "Experimental Observation of Optically Trapped Atoms". In: *Physical Review Letters* 57.3 (July 1986), pp. 314–317. DOI: 10.1103/PhysRevLett.57.314.

[21] David J. Griffiths. "Electric Fields in Matter - Polarisation". In: *Introduction to Electrodynamics*. Fourth. Boston: Pearson, 2013, pp. 167–173. ISBN: 978-0-321-85656-2.

[22] Raymond A. Serway and John W. Jewett. "26.6 Electric Dipole in an Electric Field". In: *Physics for Scientists and Engineers*. 6th ed. Belmont, CA: Thomson-Brooks/Cole, 2004, pp. 815–817. ISBN: 978-0-534-40842-8.

[23] C. J. Foot. "9.6 Theory of the Dipole Force". In: *Atomic Physics*. Oxford Master Series in Physics 7. Atomic, Optical, and laser physics. Oxford ; New York: Oxford University Press, 2005. ISBN: 978-0-19-850695-9.

[24] Rudolf Grimm, Matthias Weidemüller and Yurii B. Ovchinnikov. "Optical Dipole Traps for Neutral Atoms". In: (1999). DOI: 10.48550/ARXIV.PHYSICS/9902072.

[25] Wolfgang Ketterle and Martin W. Zwierlein. "Making, Probing and Understanding Ultracold Fermi Gases". In: *La Rivista del Nuovo Cimento* 31.506 (July 2008), pp. 247–422. ISSN: 0393697X, 0393697X. DOI: 10.1393/ncr/i2008-10033-1. arXiv: 0801.2500 [cond-mat].

[26] Michael E. Gehm. *Properties of Lithium-6*. Feb. 2003.

[27] Gaussianbeam png: en:User:DrBob. *English: Diagram of Gaussian Beam Waist Parameters*. 20 February 2009, 21:17 (UTC).

[28] Uri Levy, Yaron Silberberg and Nir Davidson. "Mathematics of Vectorial Gaussian Beams". In: *Advances in Optics and Photonics* 11.4 (Dec. 2019), pp. 828–891. ISSN: 1943-8206. DOI: 10.1364/AOP.11.000828.

[29] Rüdiger Paschotta. *Gaussian Beams*. https://www.rp-photonics.com/gaussian_beams.html.

[30] *BS EN ISO 11145:2018 - Optics and Photonics — Lasers and Laser-Related Equipment — Vocabulary and Symbols*. ISO Standard. Dec. 2018.

[31] Rüdiger Paschotta. *Beam Radius*. https://www.rp-photonics.com/beam_radius.html.

[32] Rüdiger Paschotta. *Rayleigh Length*. https://www.rp-photonics.com/rayleigh_length.html.

[33] Hannes Michael Gorniaczyk. "A Crossed Optical Dipole Trap". Diplomarbeit. Stuttgart: Universität Stuttgart, Dec. 2011.

[34] Igor Lesanovsky and Wolf von Klitzing. "Time-Averaged Adiabatic Potentials: Versatile Matter-Wave Guides and Atom Traps". In: *Physical Review Letters* 99.8 (Aug. 2007), p. 083001. DOI: 10.1103/PhysRevLett.99.083001.

[35] K. B. Davis, M. -O. Mewes and W. Ketterle. "An Analytical Model for Evaporative Cooling of Atoms". In: *Applied Physics B* 60.2 (Feb. 1995), pp. 155–159. ISSN: 1432-0649. DOI: 10.1007/BF01135857.

[36] Kendall E. Atkinson. "5.1 The Trapezoidal Rule and Simpson's Rule". In: *An Introduction to Numerical Analysis*. 2. ed. New York: Wiley, 1989, pp. 251–263. ISBN: 978-0-471-50023-0.

[37] Henning Albers. "Time-Averaged Optical Potentials for Creating and Shaping Bose-Einstein Condensates". Doctoral Thesis. Hannover, Germany: Gottfried Wilhelm Leibniz Universität Hannover, 2020.

[38] Robert G. Hunsperger. "Acousto-Optic Modulators". In: *Integrated Optics: Theory and Technology*. Ed. by Robert G. Hunsperger. Advanced Texts in Physics. Berlin, Heidelberg: Springer, 2002, pp. 175–191. ISBN: 978-3-540-38843-2. DOI: 10.1007/978-3-540-38843-2_10.

[39] D J McCarron. *A Guide to Acousto-Optic Modulators*. Dec. 2007.

[40] A. Altmeyer et al. "Dynamics of a Strongly Interacting Fermi Gas: The Radial Quadrupole Mode". In: *Physical Review A* 76.3 (Sept. 2007), p. 033610. DOI: 10.1103/PhysRevA.76.033610.

[41] Andreas von Haaren and Robin Groth. *Model of the FermiQP Assembly*. 2022.

[42] Rüdiger Paschotta. *Acousto-Optic Modulators*. https://www.rp-photonics.com/acousto_optic_modulators.html.

[43] IPG Photonics Corporation. *YLR-LP Linearly Polarized CW Lasers*. https://www.ipgphotonics.com/en/products/lasers/mid-power-cw-fiber-lasers/1-micron/ylr-lp-200-500-w. 2022.

[44] Matthias Schulz. "Tightly Confined Atoms in Optical Dipole Traps". Doctoral Thesis. Innsbruck, Austria: Leopold-Franzens-Universität Innsbruck, Dec. 2002.

[45] IPG Photonics Corporation. *Test Results: Ytterbium Fiber Laser Model YLR-200-LP-WC, S/N 22052529*. 2022.

[46] Bahaa E. A Saleh and Malvin Carl Teich. "Statistical Optics - Spectral Width". In: *Fundamentals of Photonics*. Third. Wiley, 2019, pp. 481–483. ISBN: 978-1-119-50686-7.

[47] Laser Export Co.Ltd. *Infrared (IR) CW (Continuous Wave) Diode-Pumped (DPSS) Laser for Educational and Lab Purposes - 1064 Nm*. http://laser-export.com/prod/t12.html.

[48] OZ Optics. *Polarization Maintaining Fiber Patchcords and Connectors*. Feb. 2016.

[49] Fritz Keilmann. "Precision Broadband Far-Infrared Attenuator". In: *Far-Infrared Science and Technology*. Vol. 0666. SPIE, Sept. 1986, pp. 213–218. DOI: 10.1117/12.938837.

[50] Crystal Technology, Inc. *AO Modulator Data Sheet | Model 3080-194, Part 97-02814-01, Rev B, Work Order 811190, S/N 17354*. Sept. 2011.

[51] Laser Components Germany GmbH. *Dielectric Mirror Coatings*.

[52] [SW] Yudong Sun and Yiming Feng, *Dipole Trap Codes* Aug. 2022. URL: https://gitlab.mpcdf.mpg.de/suny/dipole-trap-codes, SWHID: ⟨swh:1:dir:73a21deea7c12ee55ad0d1fd8b2ff2ab17068e98;origin=https://github.com/sunjerry019/BSc-dipole-trap-codes;visit=swh:1:snp:bc5897b1489d5652399997651fc228ee32cf2a25;anchor=swh:1:rev:d780ec76bed23208a305a7fdd0dd81ebf8a19609⟩.

[53] Janet Qesja. *Power vs. Current Set Point Measurement - IPG YLR-200-LP-WC*. July 2022.

[54] Thorlabs, Inc. *N-BK7 Plano-Convex Lenses (AR Coating: 650 - 1050 Nm)*. https://www.thorlabs.de/newgrouppage9.cfm?objectgroup_id=3280. 2022.

[55] SCHOTT AG. *N-BK7 517642.251*. https://www.schott.com/shop/advanced-optics/en/Optical-Glass/N-BK7/c/glass-N-BK7. 2022.

[56] Michael Simon. *What Is Resolution Bandwidth?* https://www.everythingrf.com/community/what-is-resolution-bandwidth. July 2019.

Acknowledgements

I would like to express my deepest gratitude to my supervisors, Prof. Immanuel Bloch, Dr. Philipp Preiß and Dr. Timon Hilker, who have generously provided knowledge, expertise and most importantly the opportunity for me to work on the FermiQP project. Their insights have been invaluable to me and the work that I have done in this thesis.

I am also grateful to my colleagues Robin, Andreas, Naman, Max, Janet, Simon, Sujay and Cady for supporting me both personally and professionally during this thesis, especially Robin and Max for the many discussions, editing help and feedback sessions. My time here in the group so far has been very enriching and often times entertaining because of the great company.

Finally, I would like to thank everyone else not mentioned here who have helped me in one way or another throughout this thesis. *Vielen Dank!*

No atoms were harmed in the making of this thesis.

Hiermit erkläre ich, die vorliegende Arbeit selbständig verfasst zu haben und keine anderen als die in der Arbeit angegebenen Quellen und Hilfsmittel benutzt zu haben.

München, den 31. August 2022
Yudong Sun